Phase Retrieval from X-Ray Intensity Measurements

David Montiel

Department of Physics

McGill University

A thesis submitted to

McGill University

in partial fulfillment of the requirements of the degree of

Doctor of Philosophy

Abstract

This thesis consists of a series of theoretical contributions to algorithmic methods for phase retrieval from diffraction intensity measurements. Our work is presented in three related, but somewhat independent parts.

The first part consists of a refinement to the phase propagation methods developed by Bates *et al.* in 1982 [1–3]. We introduce a correction term for the calculation of the phase difference between *actual* samples in reciprocal space. We show, numerically, how our method leads to improved image reconstructions in 1D.

In the second part we develop an algorithm for phase retrieval based on the Fourier series expansion of a sharp, square object support. We obtain a series of equations that describe the dependence between different points in reciprocal space, and show that this dependence becomes simpler when only a few terms of the expansion are taken into account. Our algorithm consists of two stages: In the first one, a few of the coupled equations are solved in order to obtain the phase within a localized region. This is followed by a propagation stage in which the rest of the unknown phase values are obtained by means of simple propagation method. We present a numerical example in which we use a downhill minimization method to solve the equations that arise on the first stage.

Finally, we propose a strategy for phase retrieval from x-ray diffraction measure-

ments of a system undergoing the kinetics of a first-order transition following a temperature quench. We use both, a simple theoretical model and numerical simulations to obtain an expression for the average phase-decorrelation time in ordering dynamics. We present an example to show how this result can be used to solve the phase problem faster and with higher convergence rates.

Résumé

Cette thèse consiste en une série de contributions théoriques à des méthodes algorithmiques pour la récupération de phase à partir de mesures d'intensités de diffraction. Notre travail est présenté en trois parties liées mais indépendantes.

La première partie consiste en un raffinement des méthodes de propagation de phase développée par Bates *et al.* en 1982 [1–3]. Nous introduisons un terme de correction pour le calcul de la différence de phase entre des échantillons *réels* dans l'espace réciproque. Nous montrons, numériquement, la façon dont notre méthode mène à des reconstructions d'image améliorées en 1D.

Dans la seconde partie, nous développons un algorithme pour la récupération de phase basé sur le dévelopement en série de Fourier d'un support carré. Nous obtenons une série d'équations qui décrivent la dépendance entre les différents points dans l'espace réciproque, et nous démontrons que cette dépendance devient plus simple lorsque seuls quelques termes de l'expansion sont pris en compte. Notre algorithme est composé de deux étapes: dans la première, quelques-unes des équations couplées sont résolues en vue d'obtenir la phase dans une région localisée. Elle est suivie par une étape de propagation dans laquelle le reste des valeurs de phase inconnues sont obtenues au moyen de la méthode de propagation simple. Nous présentons un exemple numérique dans lequel nous utilisons une méthode de minimisation de descente pour

résoudre les équations qui se posent sur la première étape.

Enfin, nous proposons une stratégie pour la récupération de la phase des mesures de diffusion de rayons x d'un système subissant la cinétique d'une transition de premier ordre, après une trempe. Nous utilisons un modèle théorique simple et des simulations numériques afin d'obtenir une expression du temps moyen de décorrélation de phase dans la dynamique d'ordre. Nous présentons un exemple pour montrer comment ce résultat peut être utilisé pour résoudre le problème de la phase plus vite et avec des taux plus élevés de convergence.

Acknowledgements

First of all I would like to express my most sincere gratitude to Professor Martin Grant, my supervisor for this thesis. From day one he has been incredibly supportive, and has invariably given me helpful advice and encouragement. I feel very lucky that I had the chance to work with him. Martin, I want to take this opportunity to express my respect and admiration. Thank you for everything you have done for me.

I would also like to thank Professor Mark Sutton for his invaluable contribution to this work. His insight into the subject matter and breadth of experience are both reflected in this work. Our fruitful discussions led to numerous developments described herein.

I am indebted to Paul Tupper, Dan Vernon, Rogelio Pérez-Buendia, Cristiano Dias and Chris Voyer, who generously shared their advice and expertise in different parts of this work.

I want to also thank the people I have had the opportunity to work with in the past, and who have largely contributed to my professional and personal growth. Eugenia Corvera, my MSc thesis supervisor, encouraged me to come to McGill to work on my PhD. I want to thank her for that and for all the support she has given me throughout these years. I am also very grateful to Martin Hernandez and to Vicente Talanquer, from whom I have learned so much.

I thank my mother, Cristina, my father, Héctor and my sister, Angélica for their unconditional love and support. I love you and miss you so much! I want to also thank my family and friends, too many to mention here but definitely no less important. Thank you for always being there for me. Finally, I want to thank Marie: you are my sunshine and I love you, mi corazón.

This work was supported by the Natural Sciences and Engineering Research Council of Canada, Le Fonds Québécois de la Recherche sur la Nature et les Technologies, and the Consejo Nacional de Ciencia y Tecnología (Scholarship No. 145167/193353)

.

Statement of Originality

The author claims that the following elements of this thesis constitute original scholarship and that they contribute to the advancement of knowledge.

- The derivation of a correction term used to compute the phase difference between two adjacent *actual* sampling points in reciprocal space from scattering intensity measurements of localized objects. This term was incorporated into a new phase retrieval algorithm.

- The derivation of a set of equations involving complex-valued points in reciprocal space for objects embedded in a special type of support functions. The author devised a phase retrieval algorithm based on two stages: (1) the solution of a finite subset of equations that relate to a local region reciprocal space and, (2) the propagation of this solution.

- The derivation of a theoretical model to obtain the the Fourier phase-decorrelation time in systems undergoing ordering after a temperature quench. This quantity was also obtained via numerical simulations.

- The derivation and implementation of a strategy for phase retrieval from coherent scattering intensity measurements at different times for a system undergoing ordering.

Contents

List of Figures

Chapter 1

Introduction

The work presented in thesis is intended to contribute to the field of algorithmic methods for phase retrieval from intensity measurements. This matter (also known as phase reconstruction) is raised in many fields of interest, such as astronomy, crystallography and the emerging field of diffraction microscopy. Although, for the most part this work has a general scope, it was mostly developed with the latter application in mind. In particular, we centered our attention to the problem of phase reconstruction for localized, non-periodic objects. In crystallography, the periodic nature of atoms produces strong constructive interference resulting in specific directions. As a result, localized, high intensity spots can be observed in the diffraction pattern. In contrast, non periodic objects present a more broadly distributed intensity, which require higher brilliance sources and more sensitive detectors. In addition, a high degree of coherence, both longitudinal and transverse is required to determine the specific structure of a sample. Consequently, the availability of high intensity, coherent x-ray beams produced by synchrotron sources has been crucial to the development of diffraction imaging techniques. This has also been possible due to several addi-

tional technological innovations, such as charged couple devices (CCD), employed in the construction of detectors, and modern computers, which enable the use of robust computational techniques for data manipulation. Phase retrieval algorithms, which often require a large number of numerical operations are examples of these techniques.

The nature of this thesis is theoretical. Our work consists of three related, somewhat independent contributions; each one presented in a different chapter. An outline of how content is organized is given below.

In chapter 2 we introduce basic concepts, some theory and the notation used throughout the thesis. We present an overview of the existing iterative methods for phase retrieval and discuss their application to several type of problems. We provide some examples to illustrate the advantages and limitations of most widely known algorithms. We also present a brief discuss the work of Bates *et al* [1–3] which constitutes the basis of non-iterative propagation methods. Finally we give a brief introduction to the scaling behavior that characterizes the time evolution of systems undergoing kinetics of a first order transition (ordering).

In chapter 3 we present a refinement to the phase retrieval method for oversampled intensity measurements introduced in Ref. [2]. We derive a correction term to evaluate phase differences between adjacent *actual* sampling points more precisely. We show how the inclusion of this term leads to improved image reconstructions and the reduction of error buildup in a recursive propagation scheme.

Chapter 4 contains the derivation of another method based on the solution of the phase problem in two stages. In the first one, the phase is found within a localized region in reciprocal space. The second stage consists of the recursive propagation of the solution. We take the Fourier series expansion of a sharp square support and derive a set of equations whose coupling is related to the number of terms considered

in this expansion. A minimization method is used to solve the system of non-linear equations that arises in the first stage.

In chapter 5, we introduce a strategy for phase retrieval from intensity measurements for objects representing systems undergoing ordering after a temperature quench. We show how phase reconstructions from intensity measurements of a non-equilibrium system can be achieved faster and with higher convergence rates by choosing an appropriate time interval between measurements. We support our findings by calculating phase-decorrelation times (both theoretically and numerically).

Finally, we present our conclusions in chapter 6 and briefly discuss possible related lines of work as a follow-up for the future.

Chapter 2

Background

2.1 Phase Retrieval

2.1.1 Fourier Transforms

The Fourier transform is an operation that transforms one complex-valued function of a real variable into another. Fourier transforms have applications in many fields. They are particularly helpful in signal processing and optics, where functions with oscillatory components are often encountered. We now proceed to define the Fourier transform. Let $f(x)$ be a piecewise continuous, differentiable and absolutely integrable function. The Fourier transform of f, $F(k)$ is defined as:

$$F(k) \equiv \int_{-\infty}^{\infty} f(x) e^{-ikx} dx, \tag{2.1}$$

where x and k are real variables and both f and F are, in general, complex-valued. The Fourier transform is a generalization of the Fourier series representation of a function. The variable k is usually called a wavenumber and its inverse is propor-

tional to the wavelength (λ) of the component of f represented by $F(k)$ ($k = 2\pi/\lambda$). Alternatively, the frequency, defined as $\nu = 1/\lambda = k/(2\pi)$, can be used. The Fourier transform is an invertible, linear transformation, which implies that the function $f(x)$ is recovered via the formula

$$f(x) = \frac{1}{2\pi} \int_{-\infty}^{\infty} F(k) e^{ikx} dx, \tag{2.2}$$

called the inverse Fourier Transform. This property is called completeness. In d dimensions, Eqs. (2.1) and (2.2) become, respectively,

$$F(\mathbf{k}) = \int f(\mathbf{r}) e^{-i\mathbf{k}\cdot\mathbf{r}} d^d r, \tag{2.3}$$

and

$$f(\mathbf{r}) = \frac{1}{(2\pi)^d} \int F(\mathbf{k}) e^{i\mathbf{k}\cdot\mathbf{r}} d^d k. \tag{2.4}$$

The d-dimensional analog of k, $\mathbf{k}$ is called the wave-vector. As with any complex quantity, the Fourier transform can be represented in terms of its real and imaginary parts or its modulus and phase. The latter representation (which is the one we use here) can be written in the form $F(\mathbf{k}) = A(\mathbf{k}) e^{i\phi(\mathbf{k})}$, known as Euler's formula.

2.1.2 Discrete Fourier Transforms

When a function does not exist in analytical form, but instead is approximated by a set of samples within a finite interval or region, Eqs. (2.3) and (2.4) cannot be applied directly. Instead, an approximation that involves the sampled values of the function must be used. Let there be a sequence of N values $\{f_m\} = (f_0, f_1, ..., f_{N-1})$, representing samples of the continuous 1D function f at regular intervals Δx. The

discrete Fourier transform (DFT) of F_n is also a sequence of N values and it is given by

$$F_n \equiv \sum_{m=0}^{N-1} f_m e^{-2\pi imn/N}. \tag{2.5}$$

The values f_m are recovered by applying the inverse DFT, F_n. The inversion formula is given by

$$f_m = \frac{1}{N} \sum_{n=0}^{N-1} F_n e^{2\pi imn/N}, \tag{2.6}$$

where the pre-factor $1/N$ is a normalization constant analogous to $1/(2\pi)$ in the continuous case. The values F_n represent samples on a grid in reciprocal space at intervals Δk. The sampling intervals Δx and Δk are related by

$$\Delta x \Delta k = \frac{2\pi}{N}. \tag{2.7}$$

The generalizations of (2.5) and (2.6) to higher dimensions are straightforward. It is important to keep in mind that, since only samples of the function f within a finite interval are used, the DFT is only an approximation to the Fourier Transform, and is subject to a type of distortion called aliasing. Choice of an appropriate sampling rate is key to minimizing this distortion. Equation (2.7) also shows how the sampling rate in one space is related to the size of the *total* sampling region (the whole region over which the function is sampled) in the other. The DFT can be computed efficiently in practice using a fast Fourier transform (FFT) algorithm, which reduces the number of computational steps from $\mathcal{O}(N^2)$ to $\mathcal{O}(N \log N)$ in each dimension.

In this work, we focus on two-dimensional functions and their Fourier Transforms. Since we are working with data obtained from numerical simulations, we deal with samples and we need to use DFTs. Below we show an example of a real 2D function

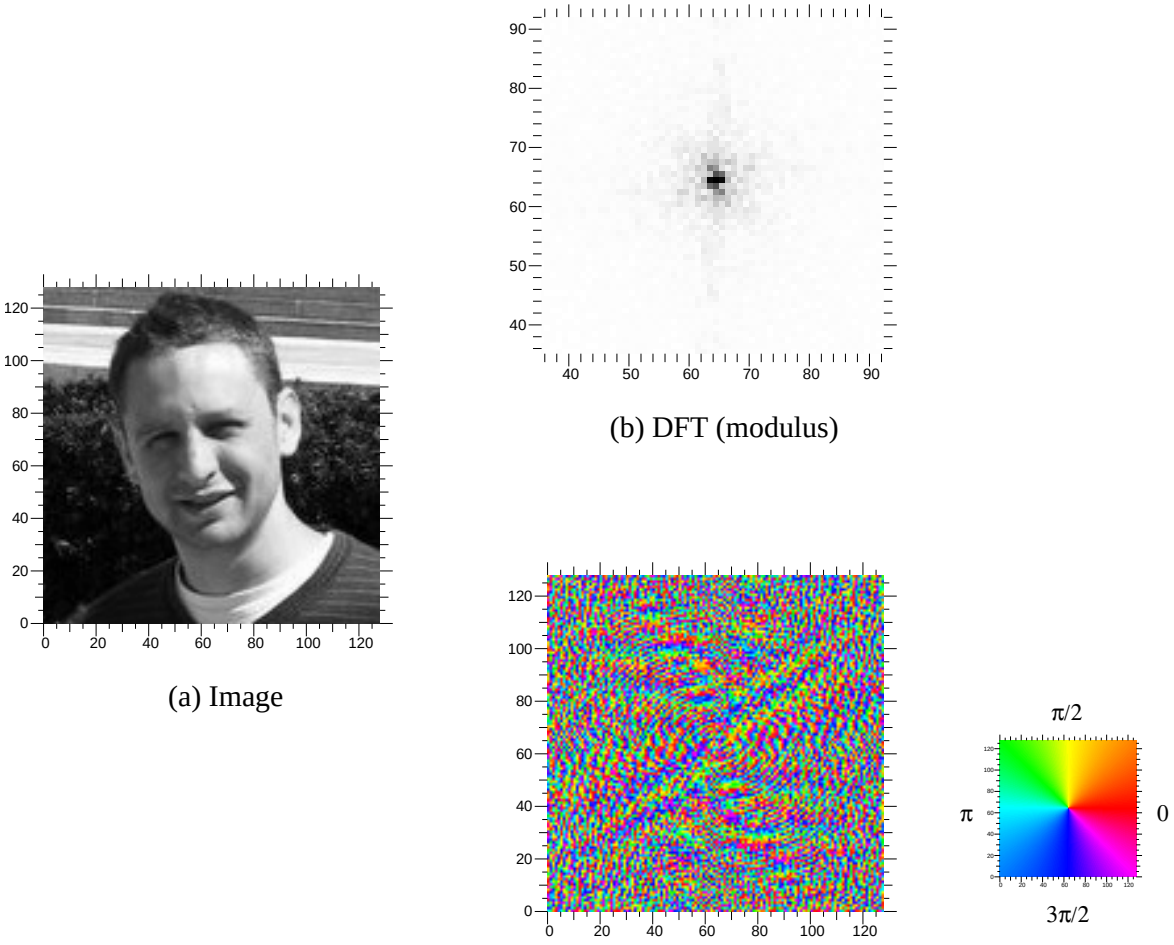

Figure 2.1: (a) A 2D real-valued function $f_{mx,my}$ represented by an image of size 64×64 pixels. The modulus (b) and phase (c) of the DFT $F_{nx,ny}$ are plotted separately. In (b) the intensity of each pixel is proportional to the modulus, with black being the maximum intensity. For (c) the values of the phase are represented by color, using the color map on the right.

in the form of a image and its DFT. We represent an image by gray-scale a pixel matrix. The intensity of each pixel is mapped to a numerical value. This is done in such a way that the maximum (white) and minimum (black) intensities correspond to the values $+1$ and -1 respectively. The two-dimensional DFT, $F_{\mathbf{n}}$, is obtained and split into two parts, modulus ($A_{\mathbf{n}}$) and phase ($\phi_{\mathbf{n}}$). Results are shown graphically in Fig. 2.1.

2.1.3 Sampling Theorem

An important result that we use extensively in this work is the Nyquist-Shannon sampling theorem. It states that if a function contains no frequency components above a certain value B, it can be completely represented by a series of equally spaced samples at intervals of size $1/(2B)$ or smaller. Such types of functions are said to be band-limited or localized in reciprocal space. Conversely, a function localized within an interval of size $2L$ can be completely represented by samples in reciprocal space taken at intervals of size $1/(2L)$ or smaller [1]. The region (in this case the interval $2L$) to which the function is localized is called support. This can also be described as the region outside of which the function is zero. The quantity $2B$ is called the Nyquist rate. What is meant by *completely represented* in this context is that one can obtain the value of a function at any point by interpolation from the samples. Mathematically, this is expressed using the Whittaker-Shannon interpolation formula shown below. Let f_m, $m = -\infty, ..., \infty$ be the set of values of a band-limited function $f(x)$ of bandwidth B, sampled at equal intervals of size $1/(2B)$. The function f(x)

[1] An important remark is that a function and its Fourier transform pair cannot be simultaneously localized; if one is localized, the other must be infinitely extended.

can then be reconstructed using

$$f(x) = \sum_{m=-\infty}^{\infty} = f_m \text{sinc}(2Bx - m), \tag{2.8}$$

where

$$\text{sinc}(t) = \frac{\sin(\pi t)}{\pi t}, \tag{2.9}$$

is called the (normalized) *sinc* function. It might be worth stressing that the sampling rate must be equal to or larger than the Nyquist rate for a function to be completely represented by its samples. Half of the sampling rate is also called the Nyquist frequency. When a function is sampled at a rate higher that the Nyquist rate it is said to be oversampled. Sampling at a rate is lower than the Nyquist rate can lead to aliasing. When this occurs, frequencies higher the Nyquist frequency are wrapped and appear as lower frequencies.

2.1.4 The phase problem

It is often the case that one is able to measure a property involving only the magnitude (modulus) of the Fourier transform of a quantity of interest. In such cases, one cannot apply an inverse Fourier transform directly because the phase is unknown. However, in many cases there is additional information available which may be enough to uniquely determine the missing phase. This matter is commonly referred to as the phase problem, and it is raised in many fields of interest, such as x-ray crystallography, x-ray, neutron or electron diffraction (which are the basis of the emerging field of diffraction microscopy and astronomy. The task of obtaining the phase information is called phase retrieval. In this context, the function representing the quantity of

interest is often called the object or the image. In x-ray diffraction experiments, for instance, the objective is to probe the microscopic structure of materials by measuring the intensity of scattered radiation in a detector. As we discuss with more detail below in section 2.2, this intensity is proportional to the squared modulus of the Fourier transform of the property that causes the scattering. In most cases, some information is available in the form of constraints that are characteristic of the object of study (*e.g.*, positivity, compactness, support, object intensity, or a combination of these). Unfortunately, even when enough is known to retrieve the phase in principle, no procedure has been developed that systematically guarantees the solution of the phase problem for all cases. However, several methods have been developed and applied with varying degrees of success.

2.1.4.1 Uniqueness

The problem of uniqueness is a crucial issue regarding the solution to the phase problem. Let, for instance, $A(\mathbf{k})$ be the true (measured) Fourier modulus. Then an object, $f(\mathbf{r})$ (with Fourier transform pair $F(\mathbf{k})$) is a solution if it simultaneously satisfies: (1) that $|F|$ is equal to the measured Fourier modulus A and (2) the complementary, known object-space constraints. Uniqueness implies that no other function g (also satisfying the object-space constraints) exists that cannot be distinguished from f based only on observation of A. In Ref. [1], Bates identifies three possible ambiguities for the phase, $\phi(\mathbf{k})$, of $F(\mathbf{k})$ called *trivial characteristics* (TC). Namely, that the quantity $\phi(\mathbf{k})$ cannot be distinguished from any of the following:

1. $\phi(\mathbf{k}) + \varkappa$, where $\varkappa$ is a real constant;

2. $\phi(\mathbf{k}) - \boldsymbol{\xi} \cdot \mathbf{k}$, where $\boldsymbol{\xi}$ is a real constant vector;

3. $-\phi(\mathbf{k})$.

These ambiguities are irresolvable when only $|F|$ is known. Fortunately they become less relevant when only the form of f is of interest, which is the case most of the time. Also, some of them can be resolved under certain types object-space constraints. Starting with TC-1, a constant term in the phase translates into a constant phase factor in the object, which has no effect in the form of f. If, in addition, the object is known to be real, the number of compatible objects is reduced to two (f and $-f$), and to one if the object is non-negative. TC-2 corresponds to a shift in origin of the object, which again, does not change the form of f. Finally, TC-3 implies indistinguishability between f and $-f^*$; once again, the form of f is unaffected. Thus, the relevant question regarding uniqueness of the solution to the phase problem is whether the form of f can be recovered uniquely from $|F|$. It turns out that the answer depends on the dimensionality of the problem. It has been shown [4, 5] that no unique solution exists for one-dimensional objects. In contrast, uniqueness for real, non-negative objects with finite support in two dimensions or more was shown theoretically by Bruck and Sodin in 1979 [5], and by Hayes [6] and Bates [1]. Later, Barakat and Newsam showed that multiplicity of solutions for complex objects is "pathologically rare".

2.1.4.2 Oversampling and support

An important result to consider in the solution of the phase problem is the fact that the square of the Fourier modulus is the Fourier transform of the autocorrelation function of the object. Mathematically we can express this as

$$\hat{R}_{ff}(\mathbf{k}) = \int R_{ff}(\mathbf{r}) e^{-i\mathbf{k}\cdot\mathbf{r}} d^d r = |F(\mathbf{k})|^2, \tag{2.10}$$

where $\hat{R}_{ff}(\mathbf{k})$ is the Fourier transform of the autocorrelation function $R_{ff}(\mathbf{r})$, defined as

$$R_{ff}(\mathbf{r}) = f(\mathbf{r}) * f^*(-\mathbf{r}) = \int f(\mathbf{x}) f^*(\mathbf{r}-\mathbf{x}) d^d x. \tag{2.11}$$

For localized objects, the autocorrelation function generally extends to an area of at most twice the size of the object in each direction, therefore is itself localized. For objects that are also non-negative, the support of the autocorrelation function can be used as an upper limit for the size of the support of an object. In this work we focus on real, strictly localized objects of tight support (meaning the size of the object is exactly known). Considering that the object is localized, the sampling theorem gives a lower bound for the sampling rate (in reciprocal space) for the object (and its Fourier Transform) to be completely determined. However, this condition applies only when both the magnitude and the phase information are sampled; yet the phase problem assumes that the latter is unknown. In Ref. [1] Bates uses the fact that the object autocorrelation can be obtained directly from the Fourier modulus to argue that one must sample at a rate of at least twice the Nyquist rate in each direction to be able to obtain the phase information; this, sampling beyond the Nyquist rate, is known as oversampling. The sampling interval in reciprocal space is proportional to the inverse of the size of the object represented in image space. As a consequence, oversampling is equivalent to extending the field of view beyond the object's support. If this is done by a factor of at least two in each direction, not only the object but its autocorrelation are represented without aliasing [2]. Another approach to oversampling is based in the notion that it leads to extra image-space information when the object support (or an estimate of it) is known, since one can then use the known "zero"

[2]The size of the autocorrelation's support cannot extend beyond twice the size (in each dimension) of the object's support

values outside the support as constraints. In 2000, Miao and Sayre [7] defined an oversampling ratio σ as

$$\sigma = \frac{\text{area of the field of view (in pixels)}}{\text{area of the object's support}}, \tag{2.12}$$

where it is assumed that all pixel values outside the support area are zero. By counting the degrees of freedom, they showed that the phase problem is undetermined unless $\sigma \geq 2$. This implies that sampling rates $\geq 2^{1/2}$ in each dimension for a 2D object and $\geq 2^{1/3}$ for a 3D object are necessary (although not always sufficient) conditions for unique reconstructions.

2.1.5 Iterative methods

The most common approach to solving the phase problem is the use of iterative methods. In these type of methods, an initial guess is iterated recursively through a succession of steps until a solution that satisfies the known constraints (both in the object and reciprocal spaces) is found. The first important contribution in this area was made Gerchberg and Saxton [8] in 1972. They developed an algorithm for phase retrieval for cases where both the Fourier and object-space magnitudes are known. Fienup [9], modified the Gerchberg-Saxton algorithm for objects applying support and non-negativity constraints. Later, he introduced a set of algorithms, amongst which the 'hybrid input-output' (HIO) is the most widely used in imaging applications [10]. Elser [11] introduced the 'difference map' and identified the Fienup algorithms as special cases of the iterated projections method. In general, for all of the algorithms mentioned above, the performance depends on the set of *a priori* constraints available for the particular type of images for which the algorithm is applied. An overview of

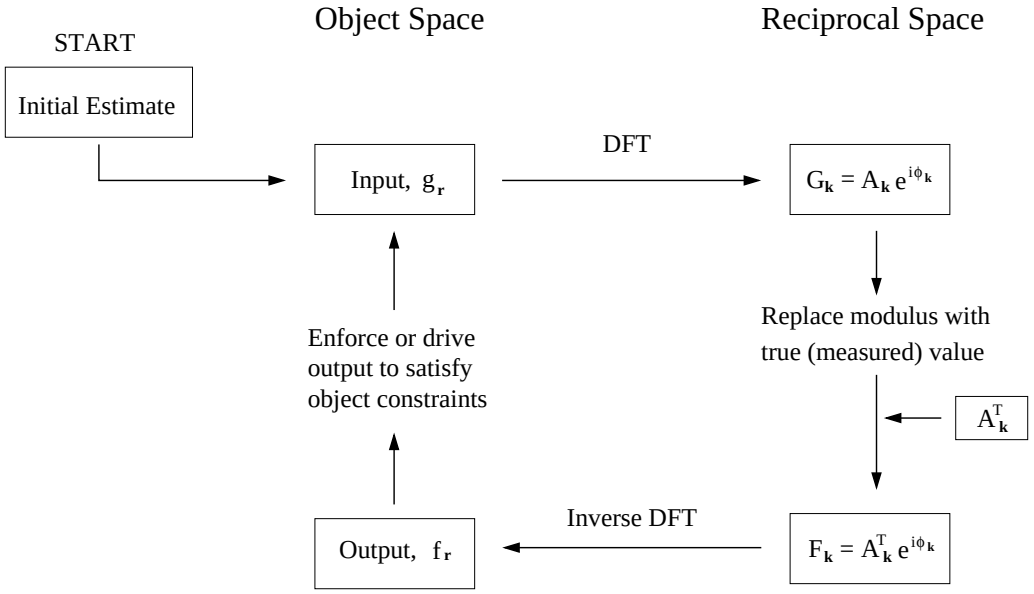

Figure 2.2: General scheme for iterative phase retrieval algorithms.

the most important methods as well as examples of their application are presented in sections 2.1.5.1 and 2.1.5.2.

In Fig. 2.2, we present a common general scheme for iterative phase retrieval methods. We represent the object and its Fourier Transform pair as an N-dimensional vectors whose components correspond to the values of N pixels in a regular d-dimensional regular grid. In addition to the Fourier modulus in reciprocal space, a set of a particular type constraints in object-space is assumed to be known *a priori*. We can identify a set of four common basic steps to each (the j-th) iteration :

1. An input $g_{\mathbf{r}}^{(j)}$, is discrete Fourier-transformed. This input is either an initial guess (for $j = 0$) or a correction involving the output from the previous iteration.

2. From the resulting complex-valued data $G_{\mathbf{k}}^{(j)}$, the modulus is discarded, replaced by the true (measured) modulus $A_{\mathbf{k}}^T$ and combined with the phase to yield new values $F_{\mathbf{k}}^{(j)}$.

3. An inverse Fourier transform is performed to get a new object $f_{\mathbf{r}}^{(j)}$.

4. A new input $g_{\mathbf{r}}^{(j+1)}$ is generated using $f_{\mathbf{r}}^{(j)}$ or a combination of both $g_{\mathbf{r}}^{(j)}$ and $f_{\mathbf{r}}^{(j)}$, in such way that that the object constraints either enforced or brought about.

The algorithm stops once a fixed point is reached, which occurs when the output does not (significantly) change between consecutive iterations. The result may or may not correspond to the solution depending on whether it simultaneously satisfies the constraints in both object and reciprocal spaces. When it does, the values $f_{\mathbf{r}}$ should correspond to the true object $f_{\mathbf{r}}^{T}$ [3], provided that the solution is unique.

Iterative algorithms have been successfully implemented in many instances. However, due to the non-convex nature of the search space, stagnation is often encountered. We present examples of this in the following sections. While there are many practical strategies to evade this problem [12], none of these guarantees that a solution can be reached within a finite amount of time starting from an arbitrary initial guess point. It has also been observed that complex valued reconstructions are noticeably harder than real-valued positive ones [13–16].

2.1.5.1 The Error-Reduction Algorithm

The Error-Reduction Algorithm is based on the Gerchberg-Saxton algorithm, which was originally developed for phase reconstruction from intensity measurements in both image and reciprocal spaces. The latter consists of four steps; the first three of them being exactly like the ones described in the previous section: An object is Fourier-transformed, the Fourier modulus is replaced by its measured value, and the result is inverse Fourier-tranformed. In the fourth step, a new estimate is obtained by

[3] Or, equivalently, $f_{-\mathbf{r}}^{*}$

also replacing the modulus in object space with the corresponding measured value. Using the same notation as the previous section, we denote the modulus and phase of output $f_{\mathbf{r}}^{(j)}$ as $a_{\mathbf{k}}^{(j)}$ and $\theta_{\mathbf{k}}^{(j)}$ respectively. If we also call the true (measured) modulus of the object, $a_{\mathbf{k}}^{T}$, then, in the fourth step, the input for a new iteration is obtained as

$$g_{\mathbf{r}}^{(j+1)} = a_{\mathbf{k}}^{T} e^{i\theta_{\mathbf{k}}^{(j)}}, \tag{2.13}$$

where $a_{\mathbf{k}}^{T}$ replaces $a_{\mathbf{k}}$. This scheme can be easily modified to be applicable to a large class of problems. In particular, cases for which a set of partial contraints in the object domain are known *a priori*. An example of this would be finite support constraints. The fourth step of the algorithm for this case takes the form.

$$g_{\mathbf{r}}^{(j+1)} = \begin{cases} f_{\mathbf{r}}^{(j)}, & \text{if } \mathbf{r} \in \mathcal{S}, \\ 0, & \text{if } \mathbf{r} \notin \mathcal{S}, \end{cases} \tag{2.14}$$

where $\mathcal{S}$ is the set of points that constitute the object's support. The fourth step, as described in 2.14 sets the input for a new iteration to be output from the previous iteration except for the region in which the object is known to be zero, *i.e.*, the object support constraints are enforced in each iteration.

The generalization of the Gerchberg-Saxton algorithm to a wider class of problems is known as the error-reduction algorithm. The correction performed in step (4) can be modified to enforce the set of constraints applicable to a particular case. In accordance with its name, the error-reduction algorithm has the property of reducing an error metric in each iteration. The convergence of this algorithm for a 2-D object is shown below.

We start by defining an error metric at the j-th iteration in the Fourier domain:

$$E_F^{(j)} = \frac{1}{N^2} \sum_{\mathbf{k}} |F_{\mathbf{k}}^{(j)} - G_{\mathbf{k}}^{(j)}|. \tag{2.15}$$

where N is the number of samples in each direction. Since the phase of $F_{\mathbf{k}}$ is the same as $G_{\mathbf{k}}$ (see Fig. 2.2), F and G only differ in modulus. Thus, when the modulus of $G_{\mathbf{k}}$ is the true modulus, steps (1) to (3) leave $g_{\mathbf{r}}$ unchanged, making the output, $f_{\mathbf{r}}$, equal to the input. As the input must satisfy the object domain constraints while the output must satisfy the Fourier domain constraints, a solution has been reached when they are equal. Note that this corresponds to the error metric defined in Eq. (2.15) being zero. A similar error metric can be defined in object space:

$$E_O^{(j)} = \sum_{\mathbf{r}} |g_{\mathbf{r}}^{(j+1)} - f_{\mathbf{r}}^{(j)}|. \tag{2.16}$$

By Parseval's theorem [17] we have

$$E_F^{(j)} = \frac{1}{N^2} \sum_{\mathbf{k}} |F_{\mathbf{k}}^{(j)} - G_{\mathbf{k}}^{(j)}|^2 = \sum_{\mathbf{k}} |f_{\mathbf{r}}^{(j)} - g_{\mathbf{r}}^{(j)}|^2. \tag{2.17}$$

We now compare Eq. (2.17) to E_O in Eq. (2.16). By definition, $g_{\mathbf{r}}^{(j)}$ and $g_{\mathbf{r}}^{(j+1)}$ must both satisfy the object constraints. Also at any point $\mathbf{r}$, $g_{\mathbf{r}}^{(j+1)}$ is the closest value to $f_{\mathbf{r}}^{(j)}$ that satisfies the object constraints ($g_{\mathbf{r}}^{(j+1)}$ is the projection of $f_{\mathbf{r}}^{(j)}$ into the object-constraints space). Then, the inequality

$$|f_{\mathbf{r}}^{(j)} - g_{\mathbf{r}}^{(j+1)}| \leq |f_{\mathbf{r}}^{(j)} - g_{\mathbf{r}}^{(j)}|, \tag{2.18}$$

must hold. We can therefore use (2.18) to compare (2.16) and (2.17)

$$E_O^{(j)} \leq E_F^{(j)}. \tag{2.19}$$

Similarly, using Parseval's theorem we have

$$E_O^{(j)} = \sum_{\mathbf{r}} |g_{\mathbf{r}}^{(j+1)} - f_{\mathbf{r}}^{(j)}|^2 = \frac{1}{N^2} \sum_{\mathbf{k}} |G_{\mathbf{k}}^{(j+1)} - F_{\mathbf{k}}^{(j)}|^2. \tag{2.20}$$

A similar argument to the one used to obtain (2.18) can be applied to the Fourier domain. $F_{\mathbf{k}}^{(j)}$ and $F_{\mathbf{k}}^{(j+1)}$ satisfy the Fourier constraints by definition; while for any value of $\mathbf{k}$, $F_{\mathbf{k}}^{(j+1)}$ is the closest value to $G_{\mathbf{k}}^{(j+1)}$ that satisfies the Fourier constraints. Therefore, we have

$$|G_{\mathbf{k}}^{(j+1)} - F_{\mathbf{k}}^{(j+1)}| \leq |G_{\mathbf{k}}^{(j+1)} - F_{\mathbf{k}}^{(j)}|. \tag{2.21}$$

Comparing (2.15) and (2.20) with the use of (2.21) we get

$$E_F^{(j+1)} \leq E_O^{(j)}. \tag{2.22}$$

Finally, combining (2.19) and (2.22), we get

$$E_F^{(j+1)} \leq E_F^{(j)}, \tag{2.23}$$

which shows that the error must either decrease or stay the same with each iteration. A condition similar to (2.22) can be obtained in terms of the error metric defined by (2.16) in the object space, making both E_O or E_F equally valid as indicators of the performance of the algorithm. Despite the fact that the error metric is monotonically decreasing, the error reduction-algorithm tends to either converge slowly or

stagnate [8, 18, 19]. In practice, its performance depends on the type of constraints imposed. Convergence seems to be reasonably fast for the problem of two intensity measurements, but very slow for the problem of single intensity measurements [10].

Below we present two examples to illustrate the application and performance of the error reduction algorithm. For both cases, we use as a sample the real valued image of size 128×128 (Fig. 2.3), and a random image as initial guess. In the first example, we run the algorithm taking the modulus of both object and Fourier as *a priori* information. In the second example, we apply support constraints by embedding the object in an area four times the size of the object. We use a normalized rms error metric defined as

$$\bar{E}_F^{(j)} = \sqrt{\frac{E_F^{(j)}}{\sum_{\mathbf{k}} |A_{\mathbf{k}}^T|^2}}. \tag{2.24}$$

The error is plotted against the number of iterations. For the two intensity problem, the convergence of the algorithm is shown in Fig. 2.4(a) and the corresponding final output image in 2.4(b). The error decreases rapidly during the first iterations, then reaches a plateau. This stagnation behaviour is typical of the error-reduction algorithm. The retrieved image is mostly correct except for a few small localized regions. Results for the finite support constraints example are shown in Fig. 2.5. As mentioned above, the fourth step of error-reduction algorithm is now given by Eq. (2.14). The error metric decreases rapidly during some stages and slowly during others. At about 1000 iterations the method stagnates. Note how the retrieved image mostly preserves the features of the true image, but appears blurry in some areas. Through these examples we have shown how, in practice, the error-reduction algorithm does not perform very well, even when it is applied to simple images like that of Fig. 2.3. We can attribute this to the fact that the Fourier modulus is a

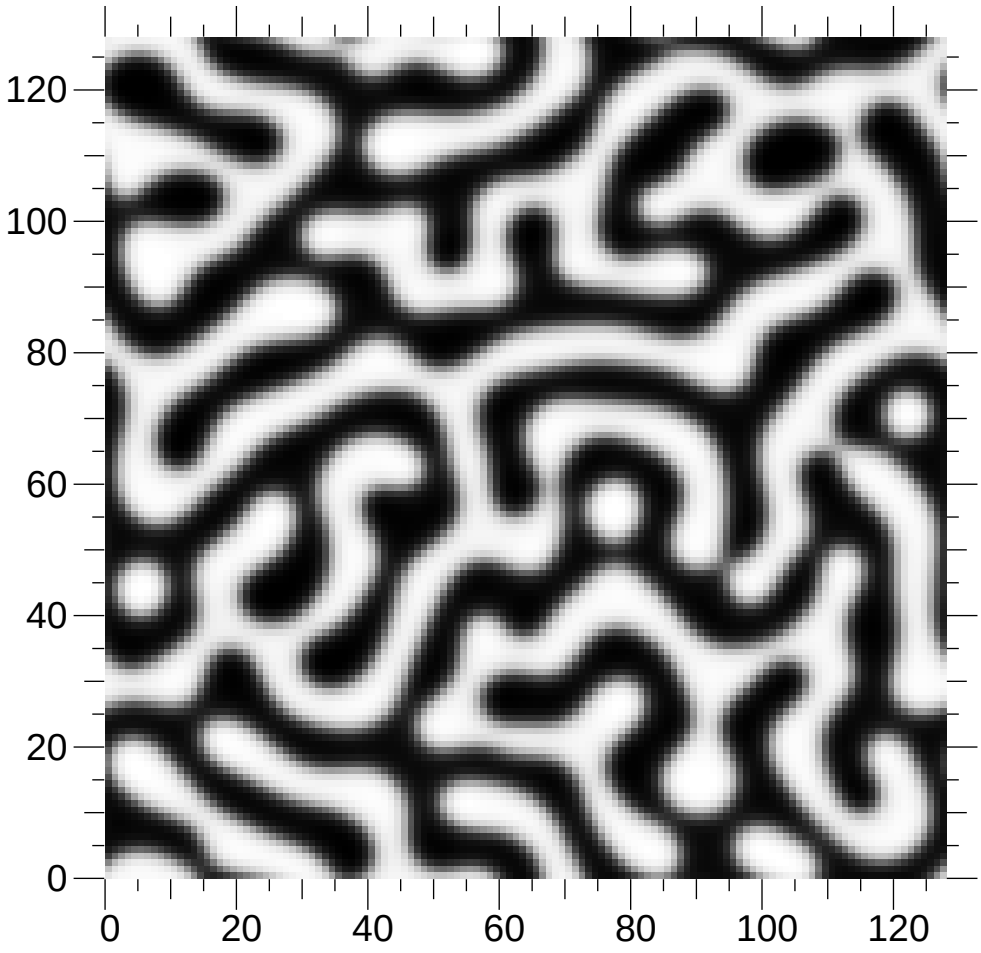

Figure 2.3: Sample image of size 128×128 pixels.

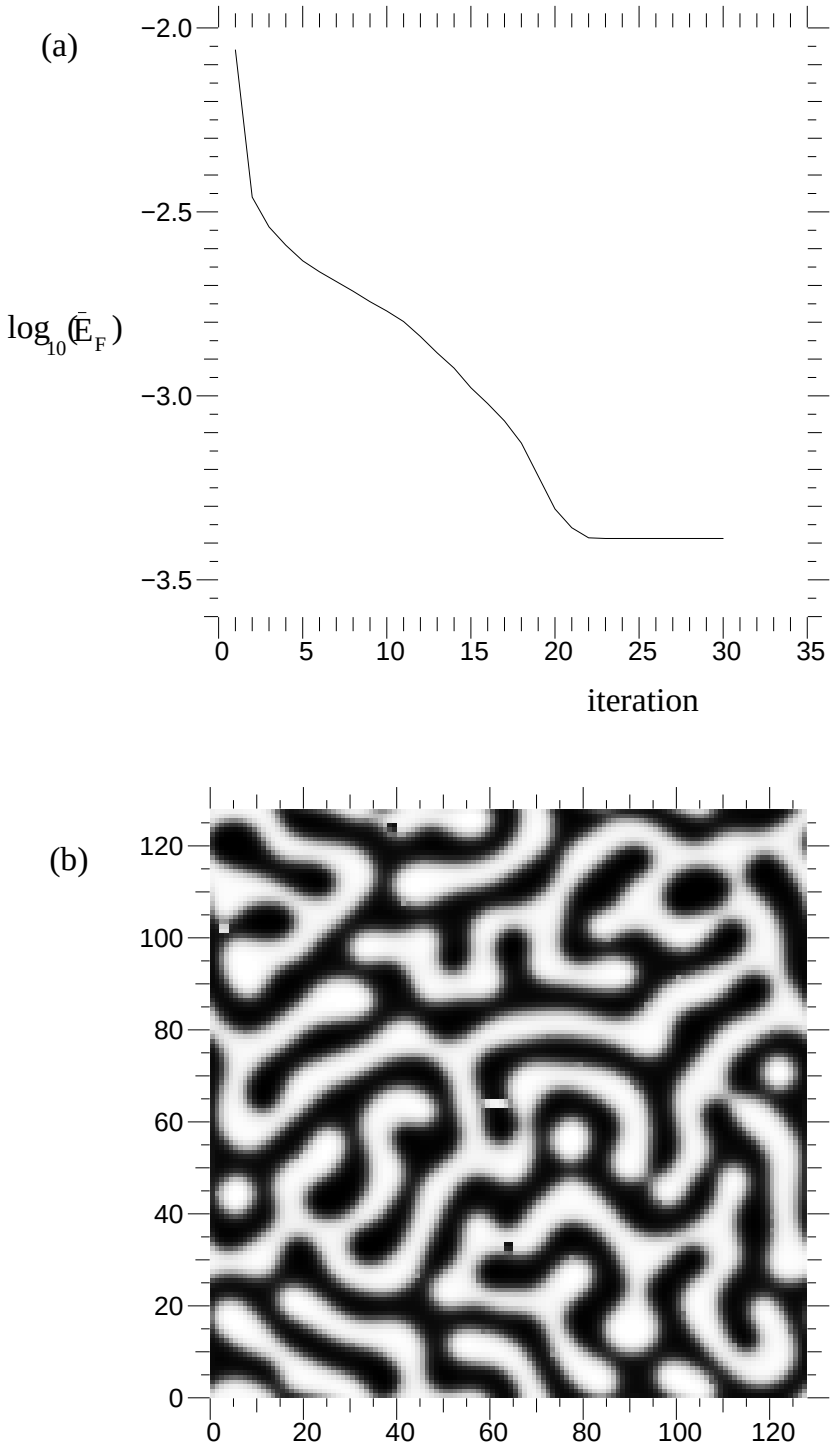

Figure 2.4: Phase retrieval for the two intensity problem using the error-reduction (Gerhberg-Saxton) algorithm. (a) Error metric vs. iteration number. (b) Retrieved image (output from the last iteration).

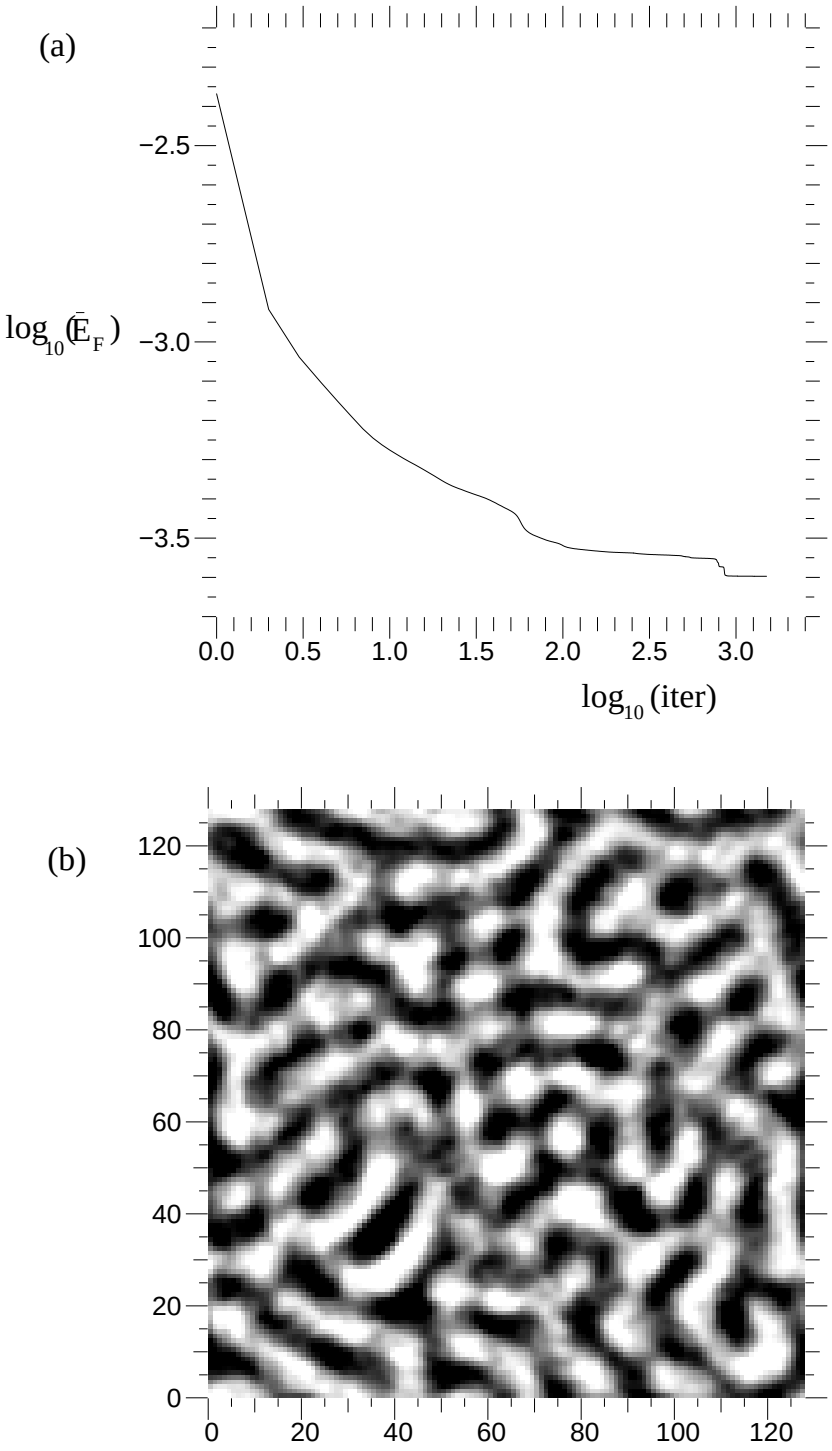

Figure 2.5: Phase retrieval using the single intensity error-reduction algorithm with support constraints. (a) Error metric vs. iteration number. (b) Retrieved image (output from the last iteration).

non-convex constraint [11]. In the following section, present an example in which we use the same image as a test for a better performing algorithm.

2.1.5.2 The Hybrid-Input Output Algorithm

The Hybrid Input-Output (HIO) algorithm belongs to a family of "input-output" methods originally devised by Fienup [10] in 1892. It has proven to be the most successful algorithm in a wide variety of imaging applications. Although, in some ways similar to the error reduction algorithms HIO also differs in important ways. First of all, unlike the error-reduction method it does not completely enforce the object constraints in every iteration. More importantly, only the output (and not the input) corresponds to the solution once a fixed point has been reached. The idea behind this method is to modify the input in each iteration in such a way that the output is driven (but not enforced) to satisfy the object constraints. In practice it only differs from the error reduction algorithm in the fourth step. Suppose that, in the j-th iteration, an input $g_{\mathbf{r}}^{(j)}$ is transformed through steps (1) to (3) into output $f_{\mathbf{r}}^{(j)}$. In general, unless a solution has been found, this output will not satisfy the object domain constraints. However, this output can be projected onto a value for which these constraints hold; we call this $c_{\mathbf{r}}^{(j)}$. In the error reduction algorithm $c_{\mathbf{r}}^{(j)}$ would be used as input for a new iteration. In the HIO algorithm, it is instead used to compute a correction to the previous input proportional to the difference $c_{\mathbf{r}}^{(j)} - f_{\mathbf{r}}^{(j)}$ at all points $\mathbf{r}$ where the object constraints are defined. For the particular case of finite object support, the new input, computed in step (4) is given by

$$g_{\mathbf{r}}^{(j+1)} = \begin{cases} f_{\mathbf{r}}^{(j)}, & \text{if } \mathbf{r} \in \mathcal{S}, \\ g_{\mathbf{r}}^{(j)} - \beta(f_{\mathbf{r}}^{(j)} - c_{\mathbf{r}}^{(j)}), & \text{if } \mathbf{r} \notin \mathcal{S}, \end{cases} \tag{2.25}$$

where β is a constant feedback parameter. Empirically, is has been found that values of β between 0.5 and 1.0 work well. Note that, for $\mathbf{r} \notin \mathcal{S}$, $c_{\mathbf{r}} = 0$, since the image is zero outside the support. We can therefore rewrite (2.25) as

$$g_{\mathbf{r}}^{(j+1)} = \begin{cases} f_{\mathbf{r}}^{(j)}, & \text{if } \mathbf{r} \in \mathcal{S}, \\ g_{\mathbf{r}}^{(j)} - \beta f_{\mathbf{r}}^{(j)}, & \text{if } \mathbf{r} \notin \mathcal{S}. \end{cases} \tag{2.26}$$

To evaluate the performance of this algorithm, a new error metric different from both E_O and E_f must be defined. The reason for this is that $g_{\mathbf{r}}$ is no longer an estimate of the image, and is not equal to $f_{\mathbf{r}}$ when the algorithm converges. Instead, a convenient measure of the error is a quantity proportional to the magnitude of the object outside the support. We define the error metric for the HIO algorithm as

$$E_{HIO}^{(j)} = \sum_{\mathbf{r} \notin \mathcal{S}} |f_{\mathbf{r}}|^2. \tag{2.27}$$

Unfortunately, it has been found that E_{HIO} does not always correlate strongly with the image quality, often making it difficult to distinguish between true and false solutions [12]. For this reason it usually a good idea to apply the algorithm repeatedly from the start, using different guesses as inputs to corroborate results. We now apply the HIO algorithm with the parameter β set to 0.7 to the sample image from the previous section (Fig. 2.3). The retrieved image as well as the convergence curve of the error metric are shown in Fig. 2.6. Once again, we use a normalized rms error metric defined as

$$\bar{E}_{HIO}^{(j)} = \sqrt{\frac{E_{HIO}^{(j)}}{N_{\mathcal{S}'}}}, \tag{2.28}$$

where $N_{\mathcal{S}'}$ is the area of the field of view outside the support, equal to the number

of terms of the sum in Eq. 2.28. We can clearly see from Fig. 2.6(a) that, although the error does not decrease monotonically, HIO converges significantly faster than the error-reduction algorithm for finite support object constraints. Also, Fig. 2.6(b) shows an image virtually identical to that of Fig. 2.3.

2.1.6 Recursive propagation

Recursive propagation methods are a particular type of non-iterative phase retrieval methods, based on the outwards propagation of the phase (in reciprocal space) from a point or region in which its value is known. The first approach of this kind was introduced by Bates *et al.* in 1982 [1–3]. They proposed a series of phase retrieval algorithms from oversampled measurements of the Fourier modulus for compact images. The work presented in chapter 3 and, to some extent, in chapter 4 roughly follows the same solution scheme. In this section, as well as in chapter 3, we use the variable frequency ν ($\boldsymbol{\nu}$ in more than one dimension) instead of wave-number k (wave-vector $\mathbf{k}$) to be consistent with the notation used in Refs. [1–3] and [20] .

The idea behind the work of Bates *et al.* is based on the principle that, for a "sufficiently" localised (as explained below) image $f(\mathbf{r})$ in d dimensions, its Fourier Transform $F(\boldsymbol{\nu})$ can be usefully represented using an expansion in sampling functions $samp_l(\boldsymbol{\nu})$ centered at points $\mathbf{p}_l$ in a regular rectangular grid called actual sampling points:

$$F(\boldsymbol{\nu}) = \sum_l F_l samp_l(\boldsymbol{\nu} - \mathbf{p}_l). \tag{2.29}$$

The value F_l is the l-th complex expansion coefficient of $F(\boldsymbol{\nu})$ and the sampling functions must satisfy

$$samp_l(0) = 1 \tag{2.30}$$

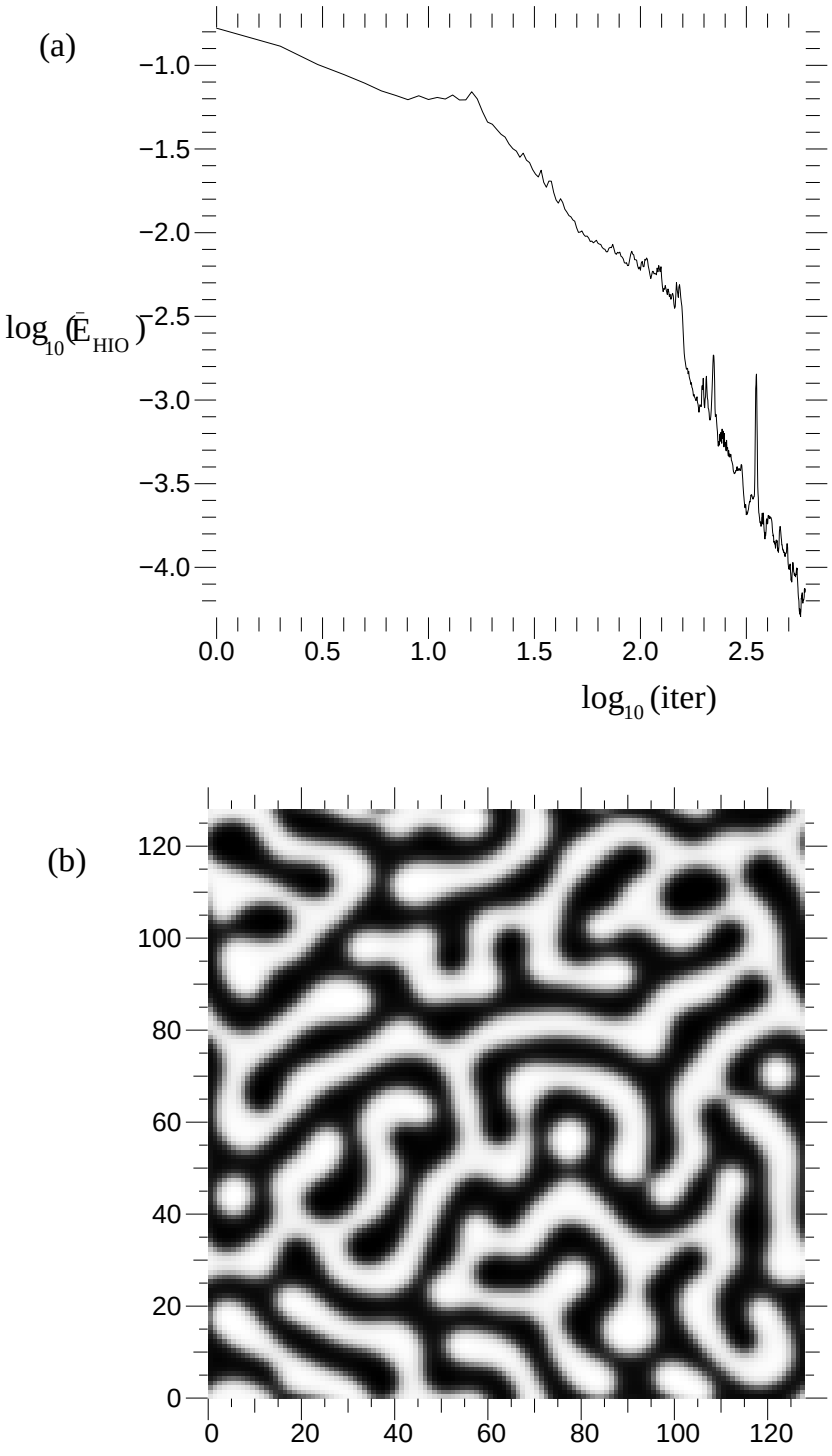

Figure 2.6: Phase retrieval using HIO with object support constraints. The feedback parameter β is set to 0.7.(a) Error metric vs. iteration number. (b) Retrieved image.

and

$$samp_m(\mathbf{p}_n - \mathbf{p}_m) = 0. \tag{2.31}$$

When the sampling functions take the form of a product (over all dimensions) of normalized sinc functions ($\mathrm{sinc}(t) = \sin(\pi t)/\pi t$), equation 2.29 becomes

$$F(\boldsymbol{\nu}) = \sum_l F_l \prod_{j=1}^{d} \mathrm{sinc}[(u_j - p_{l,j})/\alpha_j], \tag{2.32}$$

where ν_j and $p_{l,j}$ are the components in the j-th direction of $\boldsymbol{\nu}$ and $\mathbf{p}_l$ respectively. This equation is an expression for the Shannon-Whittaker sampling theorem, which, as we stated in section 2.1.3 holds when the image is strictly localized. It is important to note that Eqs. (2.30) - (2.32) are consistent only if the sample points $\mathbf{p}_l$ are located at regular intervals in a uniform rectangular d-dimensional grid, with spacing α_j, where $1/\alpha_j$ is the size of the image in the j-th direction. Therefore, the sample points can be written as $p_{l,j} = l_j\alpha_j$. From (2.30) and (2.31), we have $F(\mathbf{p}_l) = F_l$. Also important is the fact that the values F_l are proportional to the Fourier series expansion coefficients of $f(\mathbf{r})$. Thus, knowledge of the magnitude and phase of all significant values of $F(\boldsymbol{\nu})$ at a sampling rate $1/\alpha_j$, the Nyquist rate, is enough to construct both the image (using a DFT) or its Fourier Transform (using the sampling theorem). As in section 2.1.4.2, when the value of $|F(\boldsymbol{\nu})|$ (and no other *a priori* information) is available, the phase information can only be recovered by sampling at a rate higher than the Nyquist rate (oversampling). This implies that samples of values of $|F(\boldsymbol{\nu})|$ must be obtained at points that are in-between the conventional Bragg (actual) samples. For the methods described in [1–3, 21], localized, single lobed sampling functions are used instead of the infinitely extended sinc function. The use of localized functions in 2.29 implies that $f(\mathbf{r})$ can no longer be localized because the Fourier transform of a localized

function is infinitely extended. Instead, when 2.29 holds for single lobed sampling functions, the image is said to be *weakly localized* (or quasi-localized of order 1). The convenience of using single-lobed sampling functions is that it greatly simplifies 2.29. The range of the sampling functions is limited because only a few terms (values of F_l) on the right-hand side of 2.29 *survive* for any given value of $\boldsymbol{\nu}$. The method devised by Bates takes advantage of this fact and applies 2.29 with single-lobed sampling functions at values of ν located at the midpoints between actual sampling points in each direction. Note that this requires using an additional rectangular sampling grid and oversampling by a factor of at least two in each direction. The resulting equations turn out to have only a few unknowns (the phases of the actual samples) in common with each other, which makes them easier to solve numerically. Assuming the values of $|F(\boldsymbol{\nu})|$ are given for both the actual sampling points and the midpoints, one can obtain a relation between three adjacent samples (two actual, one in between) on the same line. For clarity, we will write this expression below for 1D (it is essentially the same when $d > 1$ because only samples within the same line are involved). We denote the actual samples magnitudes as $A_l = a_l^2 = |F(l\alpha)|^2$ and the in-between samples magnitudes as $B_l = b_l^2 = |F((l + 1/2)\alpha)|^2$, for integer values of l. The resulting expression is

$$B_l = \frac{1}{\zeta}(A_l + A_{l+1} + 2a_l a_{l+l}\cos(\omega_l)). \tag{2.33}$$

Here ζ is a parameter that depends on the value of the sampling function at $\alpha/2$ and ω is the phase difference between actual samples $F(l\alpha)$ and $F((l + 1)\alpha)$. In practice it makes sense to consider only a finite range of values for l (those for which the value of $|F|$ is significant). We denote $-M$ and M to be, respectively, the upper and lower limits for the index l. The value of M determines the resolution at which we expect

the image to properly represented. The only unknown in 2.33 is ω_l, so this equation can be used to compute the magnitudes of the phase difference between adjacent actual samples. As explained in detail in [1], these values can be used to obtain the phases at the actual sampling points for $d \geq 2$. The only obvious limitation for this method is that (as mentioned above) it is applicable only to weakly localized images. However, a similar approach is employed in [1] to find an approximate solution for images that are effectively strictly localized, given that we are able to sample $|F(\boldsymbol{\nu})|$ at an even higher rate in each direction. It is for this particular case that we centered our attention and developed improvements upon the previous work. In particular we present refinements to the computation of the phase differences between actual samples. A detailed description of this work is presented in chapter 3.

2.2 X-Ray scattering

Scattering or diffraction can be described as the perturbation of electromagnetic radiation or particles by one or more non-uniformities in the propagation medium. This principle can be used to probe the microscopic structure of materials by measuring the deflection of a beam of (usually) electrons, neutrons or x-rays. This deflection takes place as some spatial inhomogeneity of a sample material makes the incident beam scatter in different directions. The outgoing radiation can then be directed towards a screen where a detector measures its intensity. A very simplified schematic representation of radiation scattering from a sample is shown in figure 2.7. An incident wave represented by wave-vector $\mathbf{k}_0$ is directed towards a sample. The outgoing, scattered radiation from the sample is represented by wave-vector $\mathbf{k}_f$. The scattering vector $\mathbf{k} = \mathbf{k}_0 - \mathbf{k}_f$ is proportional to the momentum transfer between the incoming

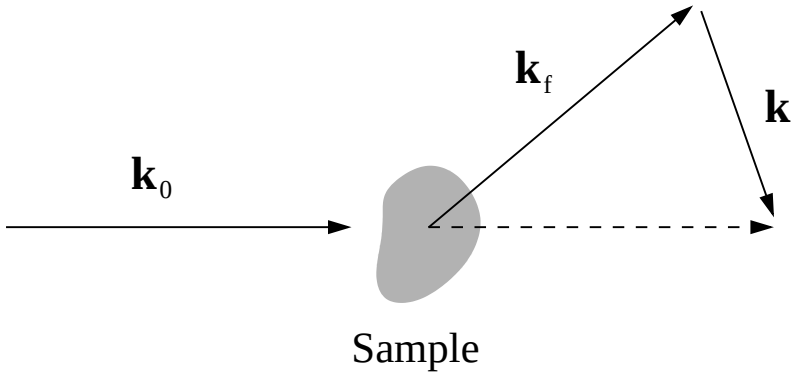

Figure 2.7: Typical geometry of a scattering experiment. An incident wave represented by wave-vector $\mathbf{k}_0$ is directed towards a sample. The outgoing, scattered radiation from the sample is represented by wave-vector $\mathbf{k}_f$. The intensity of this radiation is measured by a detector located in the back. The scattering vector $\mathbf{k}$ is defined as $\mathbf{k} = \mathbf{k}_0 - \mathbf{k}_f$

and outgoing waves. It is also proportional (in magnitude) to the distance from the origin of the diffraction pattern in the detector.

In crystallography, the fact that x-rays have a typical wavelength in the scale of nanometers, which is on the scale of covalent chemical bonds, allows for the probing of the distance between atoms and the determination of the orientation of the bonds that constitute the primitive cell. For this case, radiation is scattered by electrons and inhomogeneities in electron density are probed. Because of the periodic nature of crystals the scattered radiation from a monochromatic beam tends to interfere constructively in specific directions and destructively in all others. As a consequence, a pattern of localized high intensity spots can be observed in a detector placed far away behind the sample. These spots are known as Bragg peaks. Many inverse methods for crystallography have been developed and used successfully in the determination of crystal structures from scattered intensity measurements.

In this thesis, we are concerned with the structure of non-periodic materials. In chapter 5 we focus specifically on the study of domains formed during a phase-

transition (we call this ordering from now on) after a quench of a homogeneous system. We are therefore interested in homogeneities in the order parameter in the form of domain interfaces. Throughout this work, we assume that the scattering from these systems is elastic, i.e., no energy is absorbed or transferred to the medium. There is an additional important remark to make regarding the nature of the beam with which the sample is illuminated. Very different scattering patterns are observed depending on whether the beam is coherent or not. Coherence can be defined as the degree to which a wave is monochromatic (temporal coherence) and transversely uniform (transverse coherence). Perfectly coherent radiation propagates as a plane wave. Scattering from incoherent radiation cannot represent the detailed structure of the probed material, because different regions within a sample scatter independently, which leads to random interference. When this is the case, the measured intensity depends on an incoherent average over different regions of the scattering volume. To eliminate this incoherent average the incoming beam must have a coherence volume (the volume of the region in which the wave is both temporally and transversally coherent) larger than the size of the sample. Studies of material using ordinary (incoherent) light can therefore only measure average properties. A technical limitation for experiments involving coherent x-ray scattering of non-periodic materials is the need for high brilliance coherent x-ray sources. A high intensity source is needed because of the absence of localized, strong constructive interference regions that characterize periodic materials. Fortunately radiation from high brilliance synchrotron sources, has been available since the past two decades, allowing significant progress in the field of diffraction microscopy in recent years. This technique has been succesfully applied to imaging of non-periodic samples since 1999. The first image reconstruction was performed by measuring the soft x-ray diffraction pattern of a sample consisting

of a 2D array of gold dots [22]. Since then, two- and three-dimensional imaging of nanocrystals [23, 24] and biological samples [25–29] has been achieved.

When the incident radiation is coherent, averaging over different regions does not occur. In this case, the measured scattering intensity displays a characteristic speckled pattern. This pattern contains information about the specific structure of the sample, and not only average properties. In the Born approximation, the intensity is proportional to the magnitude of the Fourier Transform of the function that represents the inhomogeneity, like electron density, that is directly related to the structure of the sample. If we represent the property that causes the scattering as the field $\psi(\mathbf{r})$, then

$$I(\mathbf{k}) \propto |\hat{\psi}(\mathbf{k})|^2, \tag{2.34}$$

where $I(\mathbf{k})$ is the measured intensity and $\mathbf{k}$ is the scattering wave-vector. As mentioned above, the scattering intensity provides some information about the structure. However the intensity alone is insufficient to recover the precise form of this structure because the phase of the Fourier transform $\hat{\psi}(\mathbf{k})$ cannot be measured by conventional detectors. In order to obtain the real-space function $\psi(\mathbf{r})$, one needs to apply a phase retrieval method (as we mentioned in section 2.1.4) using an appropriate set of constraints. Throughout the rest of this work we consider real objects with finite support in two dimensions. Accordingly, we choose to apply the support constraint.

2.3 Ordering and scaling laws

In chapter 5 we focus on coherent scattering from systems undergoing ordering (kinetics of a first-order transition) after a temperature quench. We represent the order parameter as a continuous field $\psi(\mathbf{r})$. As we mentioned in section 2.2, the character-

istic scattering intensity pattern for these systems features rapidly fluctuating pieces, known as speckle. A typical configuration of domains undergoing ordering and their corresponding speckle patterns at a fixed time τ is shown in Fig. 2.8.

Ordering is characterised by well-known dynamic scaling behaviour, *i.e.*, patterns at two different times are statistically similar and their properties differ only by a time-dependent factor. This behavior, known as the scaling regime, usually holds for late times, where domains are well defined and interfaces are relatively sharp. The time dependence of the characteristic length R, which is the only time dependent quantity, is known to obey a power law of the form $R(t) = [B\tau]^n$, where B is a constant and n depends on the conservation laws (or absence thereof) that govern the ordering dynamics. A large number of ordering phenomena fall into two categories (called universality classes): (1) those for which the order parameter is not conserved, called model A, and (2) those for which the order parameter is conserved, model B. All of the results presented here are obtained for both of these models. The exponent, n is known to have a different value for each of these classes. Namely, 1/2 for model A and 1/3 for model B [30–32]. Examples of systems described by model A are the Ising model with flip-spin dynamics, and binary alloys undergoing an order-disorder transition. Systems described by model B include the conserved Ising model and binary alloys undergoing spinodal decomposition.

Important properties of a system can be obtained from scattering measurements. In incoherent scattering, for instance, the Fourier Transform of the density (or order parameter) correlation function is proportional to the structure factor:

$$S(\mathbf{k},\tau) = \langle I(\mathbf{k},\tau)\rangle \propto \hat{C}(\mathbf{k},\tau), \tag{2.35}$$

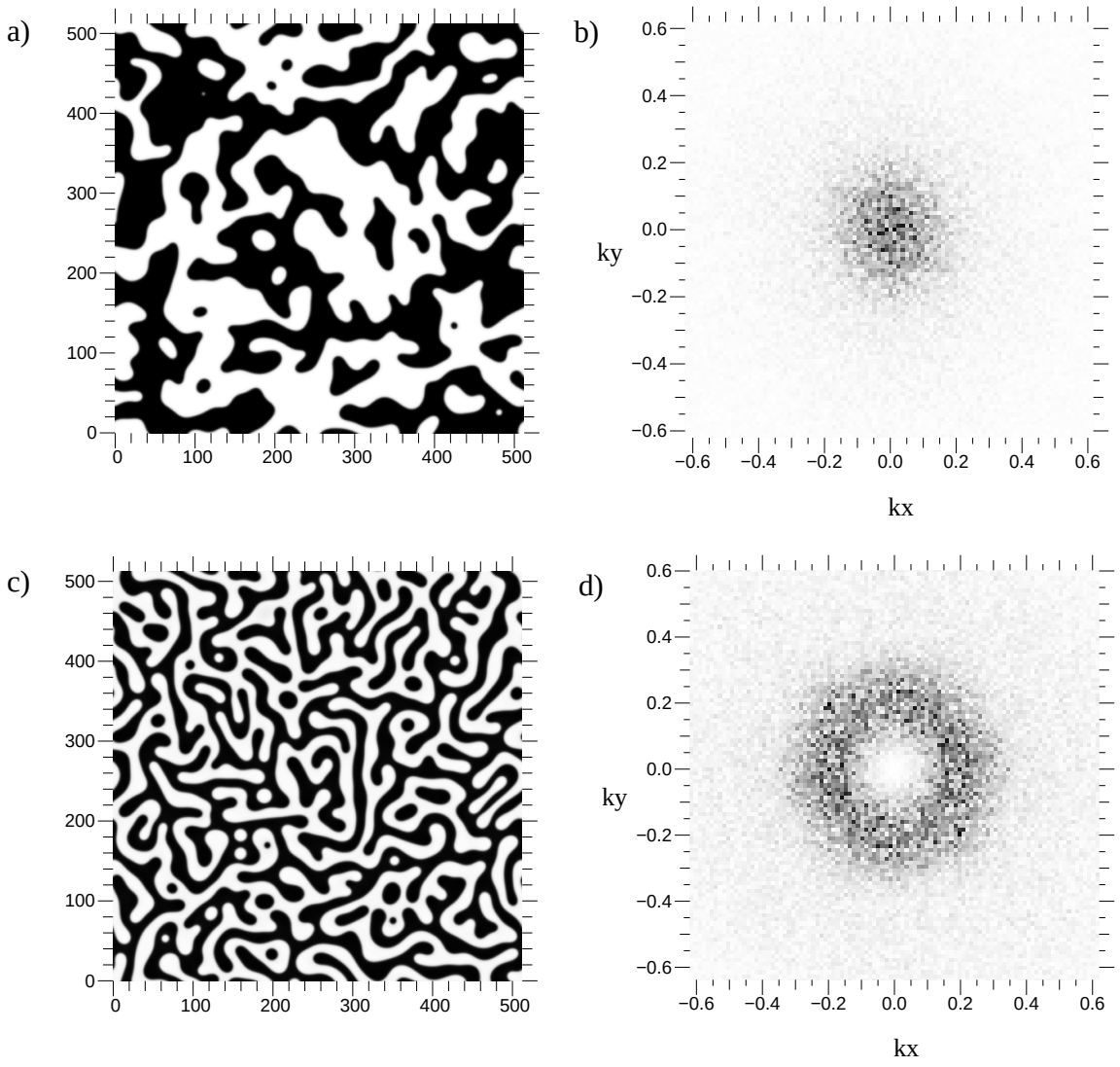

Figure 2.8: Examples of 2D ordering (numerical simulations with a grid of size 512×512) following a temperature quench. (a) Domain growth (model A) at time $\tau = 75$ (in rescaled units). (b) Speckle pattern ($\sqrt{I}$) of system (a) calculated as the modulus of its Fourier transform. (c) Spinodal decomposition (model B) at $\tau = 2000$ and (d), speckle pattern ($\sqrt{I}$) of (c).

where

$$C(\mathbf{r},\tau) = \langle \psi(\mathbf{0},\tau)\psi(\mathbf{r},\tau)\rangle. \tag{2.36}$$

The brackets in Eqs. (2.35) and 2.36 denote ensemble average over initial conditions, which is a way of simulating incoherent scattering. If a system is isotropic then all average properties depend only on the magnitude of the wave-vector $k = |\mathbf{k}|$. When the scaling relation holds, one can express $S(\mathbf{k},\tau)$ in terms of a scaling function that depends only on scaled time $t \propto \tau k^{1/n}$,

$$S(k,\tau) = k^{-d} F_1(t). \tag{2.37}$$

Alternatively $S(k,\tau)$ can also be expressed in terms of a function of only the scaled wavenumber k', defined as $k' = kR(\tau) \propto k\tau^n$,

$$S(k,\tau) = R(\tau)^d F_1'(k'). \tag{2.38}$$

Equations (2.35)-(2.38) are valid for incoherent scattering, where self-averaging takes place and one cannot obtain information about the specific structure (the domains' configuration at a given time) of the system, as opposed to coherent scattering. In the latter case, phase retrieval from the measured scattering intensity is needed to obtain the order parameter field or a quantity proportional to it.

In chapter 5, we propose a phase retrieval strategy in which an algorithm (we use HIO, but this is not essential) is applied consecutively using simulated intensity data taken at different times of a single instance of ordering dynamics. As we will describe in chapter 5, by choosing appropriate time intervals in which to measure, we can improve phase retrieval by making better initial guesses, taken from previously ob-

tained solutions at "nearby" states. In other words, for a system undergoing spinodal decomposition or domain growth, we propose the use of intensity "snapshots" taken at sufficiently short time intervals to facilitate phase retrieval when the solution at one or more of these times is known.

Chapter 3

Phase retrieval by propagation

In this chapter we introduce an algorithm for phase retrieval based on improvements to the methods developed by Bates *et al.* [1–3]. Specifically, we develop a more precise way of calculating phase differences between adjacent *actual* sampling points. This leads to a reduction in the error buildup in a recursive phase propagation scheme. In the next two sections we present a detailed derivation of this algorithm as well as a few examples of how this method can lead to improved image reconstructions. The content of this chapter is based on the work presented in Ref. [20].

3.1 Method

As we mentioned in section 2.1.6, our main goal is to derive a series of equations to be used within an algorithm for phase reconstruction based on recursive propagation of the solution. Our method is restricted to strictly localized images. Although this method can be easily generalized to 3D images, we consider its application for 1D and 2D cases only. It is shown in [21] that there is a unique solution to the phase

problem only if it is known that the image is the most compact one compatible with the modulus of its Fourier transform (unless the image is known to be positive). We assume that this is indeed the case and that a good estimate of the support size of the image is known. For the purpose of simplicity we present most of the details of the derivation in one dimension, as the generalization for the 2D case is rather straightforward.

We begin by defining a strictly localized function $f(x)$, where x is a scalar (real) and where f can be real or complex, such that $f|(x)| = 0$ for $|x| > L$. Here L is a real, positive scalar and so $2L$ is the size of the support for f. This function can be effectively represented, within the interval $[-L, L]$ by the finite Fourier series expansion:

$$f(x) = \sum_{n=-M}^{M} C_n e^{2\pi i n x/2L}, \tag{3.1}$$

with complex coefficients, C_n given by:

$$C_n = \frac{1}{2L} \int_{-L}^{L} f(x) e^{-2\pi i n x/2L}\, dx. \tag{3.2}$$

For 1D the Shannon-Whittaker sampling theorem takes the form:

$$F(\nu) = \sum_{n=-M}^{M} F_n^{Ny} \mathrm{sinc}(2L\nu - n), \tag{3.3}$$

where $F(\nu)$ is the Fourier Transform of $f(x)$ [1]:

$$F(u) = \int_{-L}^{L} f(x) e^{-2\pi i \nu x}\, dx. \tag{3.4}$$

[1] As a reminder, we are using the variable ν (instead of k) in this chapter to be consistent with the notation used in Refs. [1–3].

Note that the interval of integration is finite since f is localized. It is also important to keep in mind that

$$F_n^{Ny} = F(n/2L) = 2LC_n. \tag{3.5}$$

We shall refer to the points located at $\nu = n/2L$ as the Nyquist sampling points and to the values F_n^{Ny} as the Nyquist samples.

Consider now a representation of f within an interval $2L'$ larger than its support, *i.e.* $L' > L$. For reasons that should be clear shortly, it is convenient to choose L' to be an integer multiple of L. Then $L' = NL$, where the integer N will be referred to as the linear oversampling ratio, as defined in [33]. Equation (3.3) is still valid if we replace L by L' because the localization of f within $2L$ implies localization within $2L'$. This gives us

$$F(\nu) = \sum_{n=-M'}^{M'} F_n \mathrm{sinc}(2L'\nu - n), \tag{3.6}$$

where $F_n = F(n/2L')$. The number of terms in the sum (now $2M' + 1$) needs to be increased proportionally with N to properly represent F. We may loosely set M' to correspond to the sampling point beyond which $|F(\nu)|$ is negligible (less than an arbitrarily small value). Note that

$$F(n/2L) = F(Nn/2L'), \tag{3.7}$$

or $F_{Nn} = F_n^{Ny}$ which means that, because N is integer, equations (3.3) and (3.6) have coefficients in common which are the Nyquist samples. To preserve the terminology employed in [1–3] the points at $\nu = n/2L'$, and the values F_n will be called actual sampling points and actual samples respectively. Finally, the values of F between actual samples are named in between samples. Before we continue, it is important

to point out that those values, F_n, that correspond to points between the Nyquist sampling points are not independent the values F_n^{Ny}. Once both the magnitude and phase for all F_n^{Ny} is fixed, the values of F_n can be obtained employing (3.3).

The idea behind using the expansion (3.6) instead of (3.3) is that we expect the samples at a finer spacing to represent $F(\nu)$ more smoothly. It makes sense then to employ (3.6) to derive an simple, approximate interpolation relation for values $F(\nu)$ between two actual sampling points. An example of such relation is:

$$F([n+1/2]/2L') \simeq \gamma\{F_n + F_{n+1}\}, \tag{3.8}$$

which yields equation (2.33) simply by squaring both sides and making the substitution $\zeta = 1/\gamma^2$. An algorithm that uses (3.8) with $\gamma = 1/2$ is derived in [21]. As we mentioned in the previous section, equation (2.33) can be used to estimate $|\omega_n|$ provided we oversample enough to measure at actual as well as at in between sampling points. The value of γ is not fixed. In [2, 3] it is chosen to be the value that minimizes certain error metric, calculated after the phase has been computed. An obvious disadvantage of this approach is that one has to apply the reconstruction algorithm many times for different values of γ until the "best" reconstruction is found. Below we take a different approach, one that yields a value that depends only on the linear oversampling ratio, N.

We proceed by evaluating the error made by using the simple interpolation relation (3.8). To maintain some consistency with the notation used in [1–3] we continue to use the notation introduced in section 2.1.6 for the actual and in between samples,

now evaluated with the sampling interval $1/2L'$:

$$F_n = a_n e^{i\theta_n} \tag{3.9}$$

and

$$B_n = b_n^2 = |F([n+1/2]/2L')|^2, \tag{3.10}$$

where θ_n is the phase of the actual sample, $F(n/2L')$. We define an error function E_n at each of the in between sampling points as

$$E_n = \cos(\omega_n^{true}) - \cos(\omega_n^{est}), \tag{3.11}$$

where ω^{true} is the exact relation for the phase difference between two adjacent actual samples and ω^{est} is the estimate that satisfies the approximate relation (3.8). The two terms in (3.11) are then given by:

$$\cos(\omega_n^{true}) = \frac{F_n F_{n+1}^* + F_n^* F_{n+1}}{2a_n a_{n+1}} \tag{3.12}$$

and

$$\cos(\omega_n^{est}) = \frac{\zeta B_n - A_n - A_{n+1}}{2a_n a_{n+1}}. \tag{3.13}$$

Considering the fact that the truly independent variables are the Nyquist samples or, more precisely, the phases at the Nyquist samples, we write all the terms in both

(3.12) and (3.13) in terms of the expansion given by equation (3.3). This gives us

$$A_n = \sum_{j=-M}^{M} \sum_{k=-M}^{M} a_j^{Ny} a_k^{Ny} c_{j,k}^{Ny} \times \mathrm{sinc}(\varepsilon_{j,n} - \epsilon)\mathrm{sinc}(\varepsilon_{k,n} - \epsilon), \tag{3.14}$$

$$A_{n+1} = \sum_{j=-M}^{M} \sum_{k=-M}^{M} a_j^{Ny} a_k^{Ny} c_{j,k}^{Ny} \times \mathrm{sinc}(\varepsilon_{j,n} + \epsilon)\mathrm{sinc}(\varepsilon_{k,n} + \epsilon), \tag{3.15}$$

$$B_n = \sum_{j=-M}^{M} \sum_{k=-M}^{M} a_j^{Ny} a_k^{Ny} c_{j,k}^{Ny} \times \mathrm{sinc}(\varepsilon_{j,n})\mathrm{sinc}(\varepsilon_{k,n}), \tag{3.16}$$

and

$$\cos(\omega_n^{true}) = \frac{1}{a_n a_{n+1}} \sum_{j=-M}^{M} \sum_{k=-M}^{M} a_j^{Ny} a_k^{Ny} c_{j,k}^{Ny} \times \mathrm{sinc}(\varepsilon_{j,n} + \epsilon)\mathrm{sinc}(\varepsilon_{k,n} - \epsilon). \tag{3.17}$$

We have defined $\epsilon = 1/2N$. For all the expressions above, the variables with the superscript Ny correspond to values at the Nyquist sampling points. The matrix elements $c_{j,k}^{Ny}$ are defined as the cosine of the phase difference between the Nyquist samples j and k,

$$c_{j,k}^{Ny} = \cos(\theta_k^{Ny} - \theta_j^{Ny}). = \cos(\omega_{j,k}^{Ny}) \tag{3.18}$$

We have also defined the quantity $\varepsilon_{j,n}$ to be proportional to the distance that separates the in between sampling point $\nu = [n + 1/2]/2L'$ and the Nyquist sampling point

$\nu = j/2L$:

$$\varepsilon_{j,n} = [n + 1/2]/N - j. \tag{3.19}$$

We now substitute (3.14)-(3.16) into (3.13) and then (3.13) and (3.17) into (3.11) to get:

$$\begin{aligned} E_n = \frac{1}{a_n a_{n+1}} \Bigg(& \sum_{j=-M}^{M} \sum_{k=-M}^{M} a_j^{Ny} a_k^{Ny} c_{j,k}^{Ny}\, \Omega(\varepsilon_{j,n}, \varepsilon_{k,n}, \epsilon) \\ & + \left(2 - \frac{\zeta}{2}\right) B_n \Bigg), \end{aligned} \tag{3.20}$$

where Ω is defined as

$$\begin{aligned} \Omega(\varepsilon_1, \varepsilon_2, \epsilon) = & \frac{1}{2} \left[\mathrm{sinc}(\varepsilon_1 + \epsilon) + \mathrm{sinc}(\varepsilon_1 - \epsilon)\right] \\ & \times \left[\mathrm{sinc}(\varepsilon_2 + \epsilon) + \mathrm{sinc}(\varepsilon_2 - \epsilon)\right] \\ & + 2\mathrm{sinc}(\varepsilon_1)\mathrm{sinc}(\varepsilon_2). \end{aligned} \tag{3.21}$$

Since, in principle we can make ϵ to be arbitrarily small, it makes sense to approximate Ω by a truncated series of powers of ϵ. Because $\Omega(\varepsilon_1, \varepsilon_2, 0) = 0$ and $\Omega(\varepsilon_1, \varepsilon_2, \epsilon) = \Omega(\varepsilon_1, \varepsilon_2, -\epsilon)$ the first non vanishing them is quadratic. Thus, for small ϵ (large N) we have:

$$\begin{aligned} \Omega(\varepsilon_1, \varepsilon_2, \epsilon) \simeq & -\epsilon^2 \Big(\mathrm{sinc}(\varepsilon_1) \left[\pi^2 \mathrm{sinc}(\varepsilon_2)\right. \\ & \left. + (2/\varepsilon_2^2) \left(\cos(\pi\varepsilon_2) - \mathrm{sinc}(\varepsilon_2)\right)\right] \\ & + \mathrm{sinc}(\varepsilon_2) \left[\pi^2 \mathrm{sinc}(\varepsilon_1)\right. \\ & \left. + (2/\varepsilon_1^2) \left(\cos(\pi\varepsilon_1) - \mathrm{sinc}(\varepsilon_1)\right)\right]\Big). \end{aligned} \tag{3.22}$$

Note that, since the next term in the series is proportional to ϵ^4, (3.22) is a reasonably

good approximation for values of N as small as ~ 4. Substituting in (3.20) and using (3.16) we get:

$$\begin{aligned} E_n = &\frac{1}{a_n a_{n+1}} \left(\frac{1}{2N^2} \sum_{j=-M}^{M} \sum_{k=-M}^{M} a_j^{Ny} a_k^{Ny} c_{j,k}^{Ny} \right. \\ &\left. \times \operatorname{sinc}(\varepsilon_{j,n}) J(\varepsilon_{k,n}) + \left[2 - \frac{\zeta}{2} - \frac{\pi^2}{2N^2} \right] B_n \right), \end{aligned} \tag{3.23}$$

where J is defined as

$$J(\varepsilon) = (2/\varepsilon^2)(\operatorname{sinc}(\varepsilon) - \cos(\pi\varepsilon)). \tag{3.24}$$

Note that, at the limit $N \to \infty$, $E_n = 0$ for $\zeta = 4$. Our goal is now to find an approximate expression for E_n that does not depend on all of the unknown values $c_{j,k}^{Ny}$ and then substitute this expression into (3.11) to improve the calculation of $|\omega_n|$.

It it straightforward to notice that equation (3.23) can be simplified by choosing the value of ζ that makes the coefficient in square brackets vanish. We set then the value of ζ to

$$\zeta = 4 - \pi^2/N^2. \tag{3.25}$$

The function $J(\varepsilon)$ is shown in Fig. 3.1. Since its envelope decays much faster than the sinc function, a reasonable approximation is to truncate it into a single-lobed function. We define:

$$J_{sl}(\varepsilon) = \begin{cases} J(\varepsilon) & \text{for } |\varepsilon| \le 1 \\ 0 & \text{for } |\varepsilon| > 1 \end{cases} \tag{3.26}$$

Using $J_{sl}(\varepsilon)$ instead of the infinitely extended $J(\varepsilon)$ greatly simplifies equation (3.23). For fixed n, the values $\varepsilon_{k,n}$ are discrete and equally spaced at intervals of unit size. This implies that at most two terms in the sum over index k in equation (3.23) can

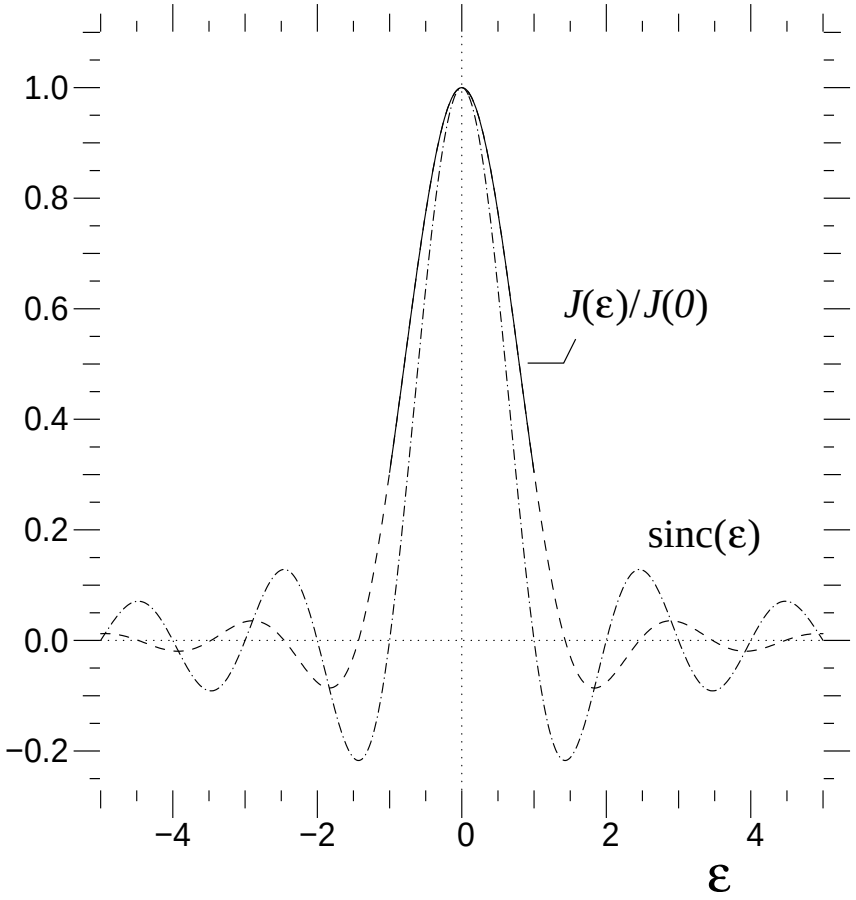

Figure 3.1: Functions $\mathrm{sinc}(\varepsilon)$ (dash-dot line), $J(\varepsilon)$ (dashed line) and $J_{sl}(\varepsilon)$ (solid line), truncated to zero outside the interval $[-1, 1]$.

survive. Substituting J_{sl} into (3.23) and the result into (3.11) we get:

$$\cos(\omega_n^{corr}) = \cos(\omega_n^{lin}) + \frac{b_n}{2N^2 a_n a_{n+1}} \Big[a_j^{Ny} c_{j,n} J_{sl}(\varepsilon_{j,n}) + a_{j+1}^{Ny} c_{j+1,n} J_{sl}(\varepsilon_{j,n} - 1) \Big]. \tag{3.27}$$

Here, j is the index of the closest Nyquist sample to the left of actual sampling point n. We define the coefficient $c_{j,n}$ as:

$$c_{j,n} = \cos\left(\theta([n + 1/2]/2L') - \theta_j^{Ny} \right). \tag{3.28}$$

We have also renamed ω_n^{est} as ω_n^{lin} to stress that it corresponds to estimate obtained using the linear interpolation formula (3.8). The term in square brackets in (3.27) represents a correction to the simple interpolation relation (3.13). Accordingly, we will refer to it as the *correction* term.

The only unknown quantities in (3.27) are $c_{j,n}$ and $c_{j+1,n}$, which depend on the phase differences between the point $\nu = [n + 1/2]/2L'$ and the nearest Nyquist sampling points to the left and the right. Both of these quantities can be approximated using the following general scheme: By performing a preliminary phase propagation from Nyquist sampling point ν_j^{Ny} to point ν_{j+1}^{Ny} we can find an estimate for θ_{j+1}^{Ny}. This can be done using (3.13) (which does not depend on any unknown variables) to get estimates of $|\omega_n|$. (In the 1D case, the signs of $|\omega_n|$ must be known *a priori* for the phase to be unique [2]. For the 2D case, the signs can be obtained unambiguously using

[2]The solution to the phase problem is not unique in 1D. In the most general case (for a complex image), there can be up to 2^{2M-1} different sets of phases compatible with a set of $2M + 1$ given magnitudes a_l. This is consistent with the fact that there are two possible choices for the sign of each phase difference (ω_l) between adjacent samples [1].

the method described in [1].) Since we started at point ν_j^{Ny}, θ_j^{Ny} is assumed to be already known (or estimated). Then we can use the following expression to estimate θ at all the in between sampling points between ν_j^{Ny} and ν_{j+1}^{Ny}:

$$\theta\left(\frac{n+1/2}{2L'}\right) \simeq \text{ phase}\left\{F_n + F_{n+1} - \frac{1}{4N^2}\left[F_j^{Ny} J_{sl}(\varepsilon_{j,n}) + F_{j+1}^{Ny} J_{sl}(\varepsilon_{j,n}-1)\right]\right\}. \tag{3.29}$$

The equation above can be obtained through a similar derivation as the one that leads to (3.27), applied to equation (3.8) instead of (3.13). Finally, we can use (3.27) with the estimates obtained in the previous step to repeat the propagation between the two Nyquist sampling points. This should give us better estimates, and so we can repeat the propagation with the updated estimates until we get a stationary solution. It is important to mention that for the 2D phase propagation this must be done simultaneously for each row and column of actual points within a Nyquist cell. Thus estimates for the phase must be computed not only at the Nyquist points on the corners but also on the sides of the Nyquist cell. This scheme is illustrated in Fig. 3.2. The values of the phase at the actual sampling points on all sides of the Nyquist cell are estimated on the preliminary propagation. These values are then used to estimate the phases of all the in between points with of (3.29) applied to all rows and columns. The propagation is repeated until a steady solution is found. Once the solution for the first Nyquist cell has been computed. The rest of the solution can be found by outwards propagation for the remaining Nyquist cells, with the procedure described above repeated for each cell. The values of the phases at the Nyquist sampling points, with the corresponding known amplitudes, are sufficient to compute the form of the retrieved image function using (3.1). The complete phase retrieval scheme is outlined

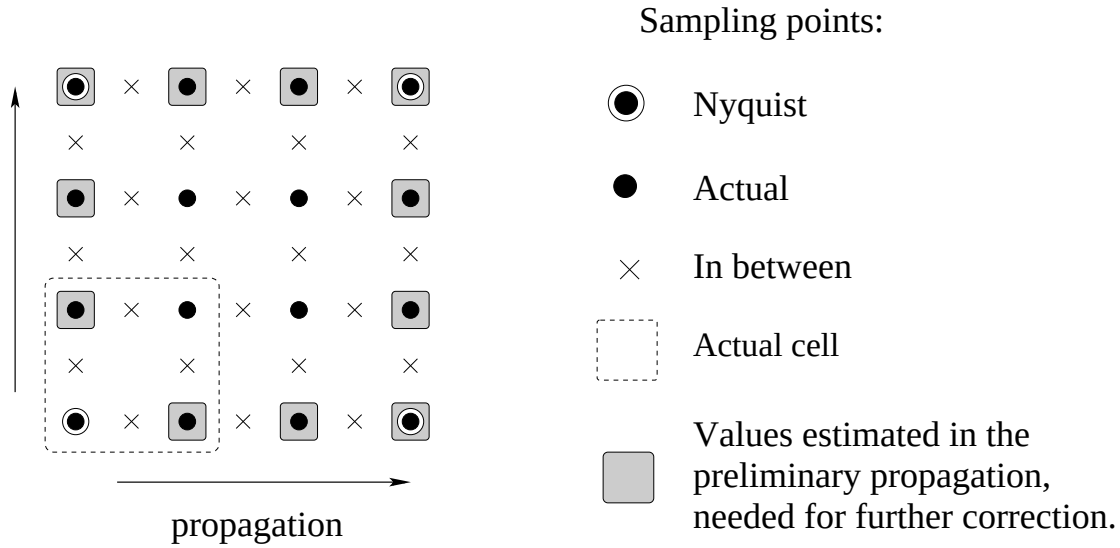

Figure 3.2: Propagation scheme in 2D within a single Nyquist cell. The phase is propagated at each actual cell (any square formed by four adjacent black dots) from the lower-left corner to the upper-right corner of the Nyquist cell. The values of the phase at the edges (marked with squares) need to be updated at each subsequent propagation that includes the correction term. The propagation in each Nyquist cell is iterated until a steady solution is reached. In the 1D case the propagation is done within single line (left to right).

in Fig. 3.3.

3.2 Results

We present a few examples of the method described in the previous section. We first consider phase propagation in 1D. We construct a sample that consists of a real, strictly localized image $f(x)$ of support size equal to unity. We take this image to be effectively represented within the interval $[-1/2, 1/2]$ as a Fourier series of finite (a few) number of terms $(2M + 1)$. This gives us:

$$f(x) = \sum_{n=-M}^{M} C_n e^{2\pi i n x}, \tag{3.30}$$

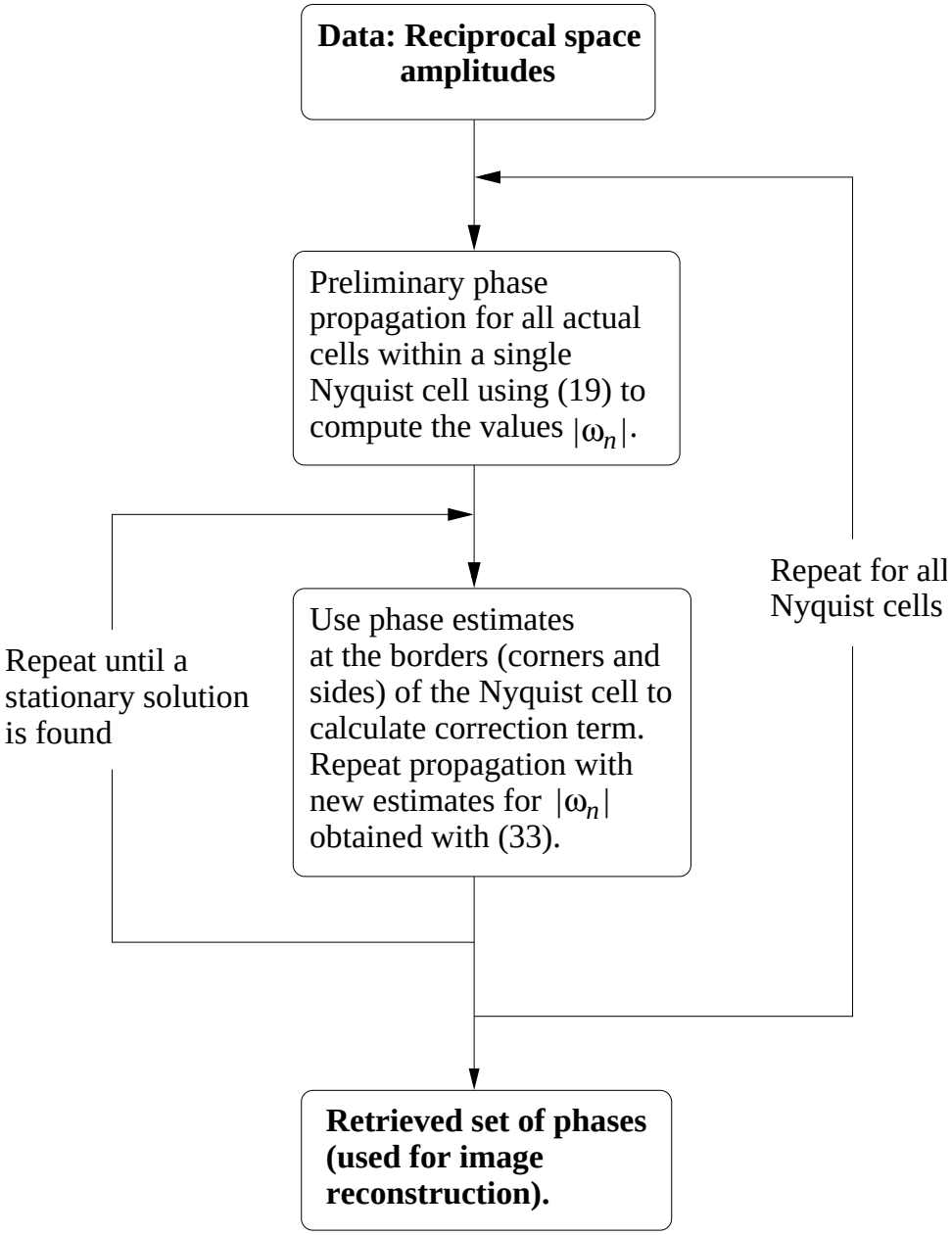

Figure 3.3: General scheme for phase retrieval.

where $C_n = F_n^{Ny} = a_n^{Ny} \exp\left(i\theta_n^{Ny}\right)$. Since f is real, Friedel's Law requires that $C_n = C_n^*$, which implies than only $M+1$ coefficients in (3.30) can be fixed arbitrarily. For the sample images we show in Fig. 3.4, we fixed the value of M to $M = 8$, *i.e.* we take 8-component images. We use a half-normal distribution with variance $\sigma^2 = 1$ to generate the amplitudes of the $M + 1$ independent coefficients, and a continuous uniform distribution on the interval $[0, 2\pi]$ for the phases. The phase θ^{Ny} is set to zero for the zeroth mode ($j = 0$). The constructed sample functions are represented by solid lines. For the calculation of the phase-retrieved functions (dashed lines) we assume knowledge of the signs of the phase differences between adjacent actual points. This information could be available from (possibly) noisy estimates (Φ_n) of such phase differences obtained externally [34]. Then a recursive phase correction method, in which the only signs of phase difference estimates are used in combination of the computed values $|\omega_n|$, should yield better results than using the values Φ_n directly, provided that the values $|\omega_n|$ are more accurate. This approach is applied (and described in more detail) in [2]. Our results, obtained using (3.27) are compared with reconstructions of the same system using Bates's interpolation relation (3.13). We call the latter Bates's images. We show examples of reconstructions for three different linear oversampling ratios: $N = 4$, 6, and 8. We found that our method works well for $N \geq 4$. For Bates's images (right), we set the parameter ζ to an optimum value via the minimization of an error criterion function defined in [2]. For our own results (left), we used the value of ζ fixed by (3.25). It can be seen from the figure that, for the cases considered our method yields consistently (although not dramatically) better results than Bates's method, with the additional advantage that our equations have no adjustable parameters.

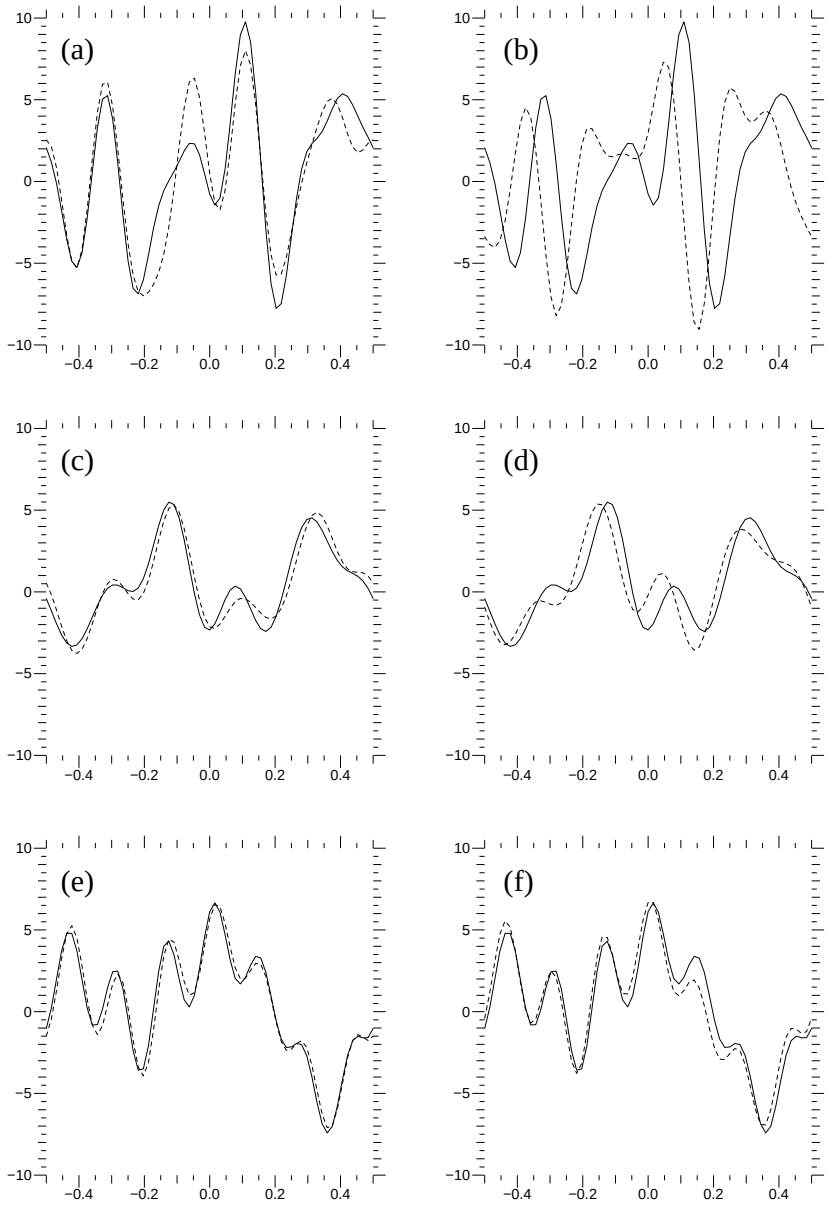

Figure 3.4: Sample eight-component images (solid lines) and reconstructed images (dashed lines). (a), (c) and (e) were obtained using the method described in section 3.1 with the correction term from (3.27). (b), (d) and (f) were obtained using Bates's method with (3.13). The (optimal) values of γ used for Bates's reconstructions are, respectively: $\gamma = 0.509$, $\gamma = 0.497$, and $\gamma = 0.503$. Different linear oversampling ratios were used for each reconstruction: $N = 4$ for (a) and (b), $N = 6$ for (c) and (d), and $N = 8$ (e) and (f).

Chapter 4

Localized phase retrieval

In this chapter, as with the previous one, we introduce a phase retrieval algorithm from oversampled intensity measurements in 2D. We consider an approximation to the particular case in which a real-space object is embedded in a sharp square support. We obtain the relations that describe the dependence between different points in reciprocal space when a Fourier expansion is used, and show that this dependence becomes simpler when only a few of these modes are taken into account. Within this approximation, we introduce an method that consists of two stages: In the first one a few of the values for the phase within a localized region in reciprocal space are obtained. These values are then used to obtain the rest of the unknown phase values by means of a simple propagation method on the second stage. In section 4.2 we present an example in which we use a downhill minimization method with different starting points to solve the system of non-linear equations that arises on the first stage. This chapter contains the work presented in Ref.[35]

4.1 Method

We start by defining a continuous 2-D function represented (within a finite interval) by a set of N^2 discretely sampled points $\{\psi_{\mathbf{r}}\}$. The components (x, y) of the index $\mathbf{r}$ run from 0 to $N-1$. The set $\{\psi_{\mathbf{r}}\}$ constitutes the unknown real-space object to be reconstructed. The Discrete Fourier Transform (DFT) of $\psi_{\mathbf{r}}$ is given by

$$\hat{\psi}_{\mathbf{k}} = \frac{1}{N^2} \sum_{x=0}^{N-1} \sum_{y=0}^{N-1} \psi_{\mathbf{r}} e^{-2\pi i(k_x x + k_y y)/N} = A_{\mathbf{k}} e^{i\phi_{\mathbf{k}}}, \tag{4.1}$$

where $\mathbf{k}$ runs over the same values as $\mathbf{r}$. The values $A_{\mathbf{k}}$, the moduli $\hat{\psi}_{\mathbf{k}}$, are known from intensity measurements [1] and from now on we will consider them as fixed parameters. The phases $\{\phi_{\mathbf{k}}\}$ are unknown and the solution of the phase problem lies in obtaining these phases.

We consider a system in which the object (the finite set of values $\{\psi_{\mathbf{r}}\}$) is embedded in a support whose value outside the object is known. In particular we are interested in the case where the support is zero outside the object. To represent an image beyond the object one must sample the intensity (oversample) beyond the Nyquist rate in reciprocal space. Here we consider a 2D object whose intensity is oversampled by exactly a factor of 2 in each dimension; this corresponds to a system where the support is 4 times as big as the object. We set its size to be $(2N)^2$. An example of such a system is shown in Fig. 4.1, obtained from a simulation of non-equilibrium domain growth where the scalar order parameter is not conserved (Model A). From 4.1(b), we can observe how the oversampled the intensity appears smoother than conventional

[1] It is important to keep in mind that the DFT is only an approximation to the continuous Fourier Transform, whose square modulus is the actual quantity measured in an intensity detector. This approximation should be valid as long as the whole sampling interval in reciprocal space is chosen to be large enough so that the Fourier amplitude of wavenumbers beyond this interval is known to be sufficiently small.

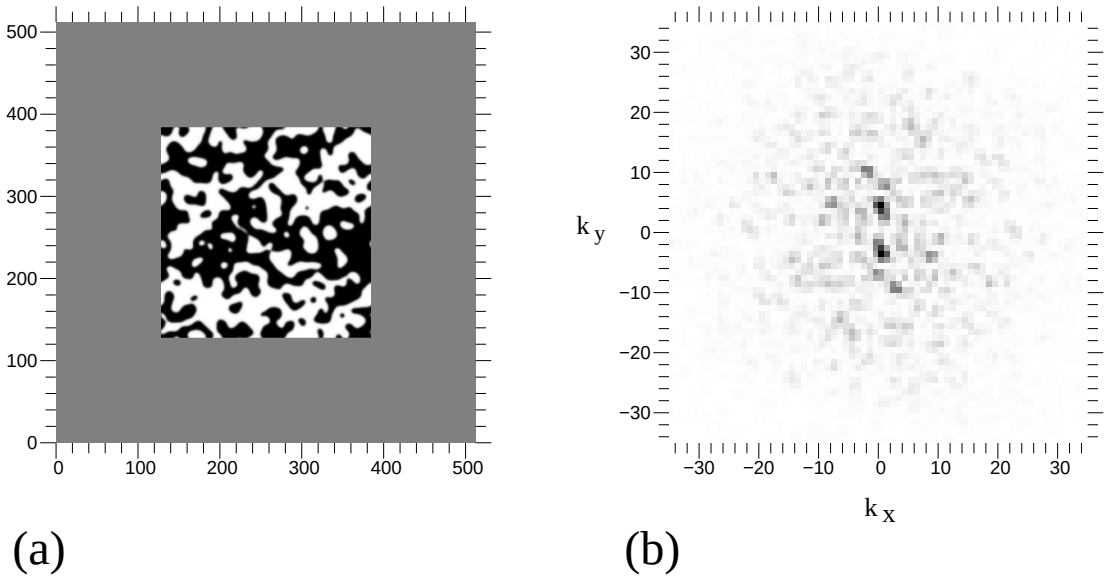

Figure 4.1: (a) A 2D object embedded in a support 4 times is size. (b) The corresponding diffraction pattern intensity; obtained by taking the DFT of (a).

Bragg sampling intensity (see Fig. 2.8).

In what follows, we show how sampling beyond the Nyquist rate in reciprocal space gives rise to known relations between Fourier modes that intrinsically carry information about the phase. The Sampling Theorem states that, given a continuous localized function (*i.e.* a function whose value is zero outside a finite interval), its Fourier Transform can be obtained from its values sampled at regular intervals whose size is given by the Nyquist rate. Mathematically we can express this the following way: Let $f(t)$ be a function that vanishes for $|t| > L$. Then $\hat{f}(\omega)$ is determined by its values at $\omega_n = n\pi/L$ by the formula

$$\hat{f}(\omega) = \sum_{-\infty}^{\infty} \hat{f}(\omega_n) \frac{sin(L(\omega - \omega_n))}{L(\omega - \omega_n)}. \tag{4.2}$$

We have considered the special case of a symmetric interval $[-L, L]$ for f but it can be shown that a similar expression to (4.2) can be obtained for any interval of size

$2L$. From the Sampling Theorem it is clear that sampling at a frequency finer than the Nyquist rate is unnecessary if one knows all the values (modulus and phase) of $\hat{f}_n = \hat{f}(\omega_n)$. However, oversampling is useful when a part of $\hat{f}_n$ (like the phase, in our case) is unknown. For this case, (4.2) provides a relation between phases of the *in-between* oversampled points and the points sampled at the Nyquist rate. For this work we consider oversampling at exactly half the Nyquist rate in each dimension. The expression obtained from (4.2) evaluated at the mid values $\omega_n + \pi/2L$ is

$$\hat{f}(\omega_n + \pi/2L) = \sum_{n'=-\infty}^{\infty} \hat{f}(\omega_{n'})\hat{g}(n - n') \tag{4.3}$$

where

$$\hat{g}(n) = \frac{(-1)^n}{\pi(n + 1/2)}. \tag{4.4}$$

In practice, we can only take a finite number of terms to compute (4.2) and therefore we must return to a discrete representation. If for each dimension we take a set of N values sampled at the Nyquist rate then by oversampling at half of the original interval we get 2N points (in each dimension). Denoting the set of oversampled points as $\hat{\psi}_{\mathbf{k}} = \hat{\psi}_{k_x,k_y}$, we call the original points *even* and the mid (oversampled) points *odd*, and we obtain the following relations as discrete analogs of Eq. (4.3) in two dimensions:

$$\hat{\psi}_{2k_x,2k_y+1} = \frac{1}{\sqrt{N}} \sum_{k_{y'}}^{N-1} = \hat{\psi}_{2k_x,2k_{y'}} \hat{g}_{k_y - k_{y'}} \tag{4.5}$$

$$\hat{\psi}_{2k_{x+1},2k_y} = \frac{1}{\sqrt{N}} \sum_{k_{x'}}^{N-1} = \hat{\psi}_{2k_{x'},2k_y} \hat{g}_{k_x - k_{x'}} \tag{4.6}$$

$$\hat{\psi}_{2k_{x+1},2k_{y+1}} = \frac{1}{N} \sum_{k_{x'}}^{N-1} \sum_{k_{y'}}^{N-1} \hat{\psi}_{2k_{x'},2k_{y'}} \hat{g}_{k_x - k_{x'}} \hat{g}_{k_y - k_{y'}}. \tag{4.7}$$

The set of N values $\hat{g}_k$, the discrete analog of $\hat{g}(n)$ is given by

$$\hat{g}_k = \frac{1}{\sqrt{N}} \frac{(-1)^k}{\tan(\pi(k+1/2)/N)}. \tag{4.8}$$

Note that, except for a constant factor, $\hat{g}_k$ and $\hat{g}(n)$ are identical for small values of k (or n). Fig. 4.2 shows the plot of $\hat{g}_k$. By examining this plot and equations (4.5-4.7) it becomes apparent how each of the *odd-even* (*o-e*), *even-odd* (*e-o*) and *odd-odd* (*o-o*) modes depend on the *even-even* (*e-e*) neighboring modes. For instance, plot 4.2 shows the way the contribution of each mode falls off as a function of distance. In any case, we could in principle use equations (4.5-4.7) to obtain the phases of $\hat{\psi}_{\mathbf{2k}}$ by taking the modulus of each equation and solving the system (which is in fact, over-specified) for the $N^2/2$ independent phases [2]. However, the problem with this approach is that the system of equations that results is nonlinear and difficult to solve for mainly two reasons: (1) the coupling of modes (given by the range of function $\hat{g}_k$) and (2) the fact that the number of unknowns ($N^2/2$, the *e-e* modes) grows as the size of the system. The approach that we take in this paper (which will be described shortly) is based on an approximation that allows us to both limit the range of interaction between modes and more importantly, limit the number of unknowns by picking a finite region in reciprocal space for which the problem is locally determined (at least in principle). The rest of the information is obtained by a propagation method that involves solving only equations of one variable.

We start by pointing out the fact that the nature of the interaction between modes depends on the shape of the support; for instance, the shape of the function $\hat{g}_k$ is specific to a perfectly squared support with sharp edges. Accordingly, we have found

[2] if the object is real, Friedel's law implies that $A_{\mathbf{k}} = A_{\mathbf{2N-k}}$ and $\phi_{\mathbf{k}} = -\phi_{\mathbf{2N-k}}$.

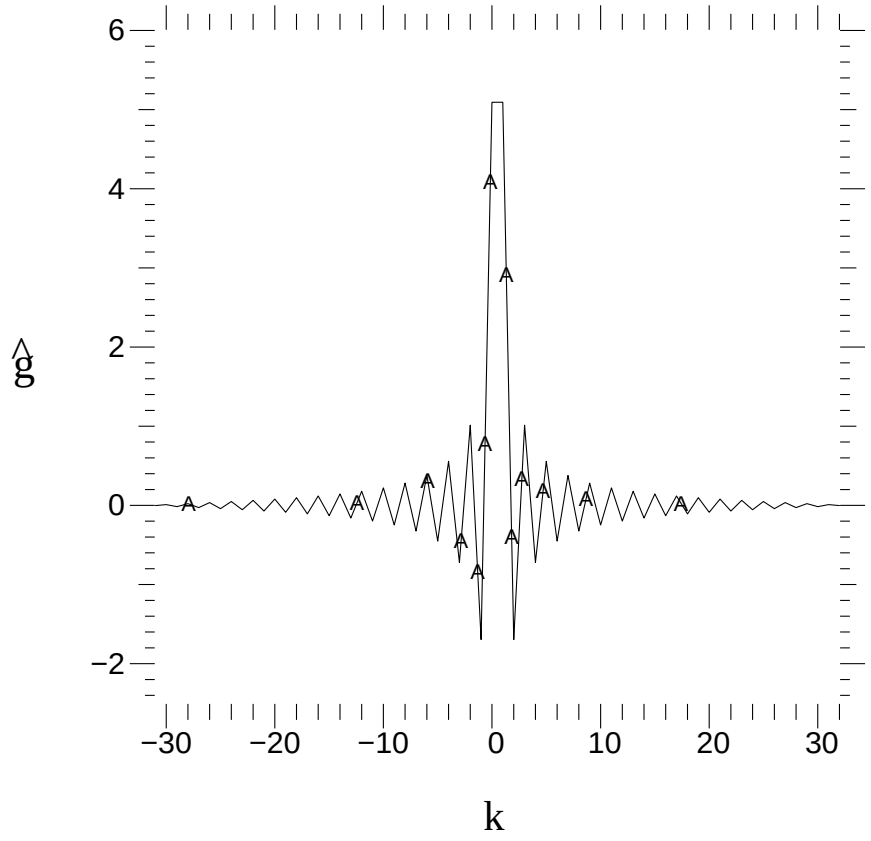

Figure 4.2: Plot of function $\hat{g}_k$.

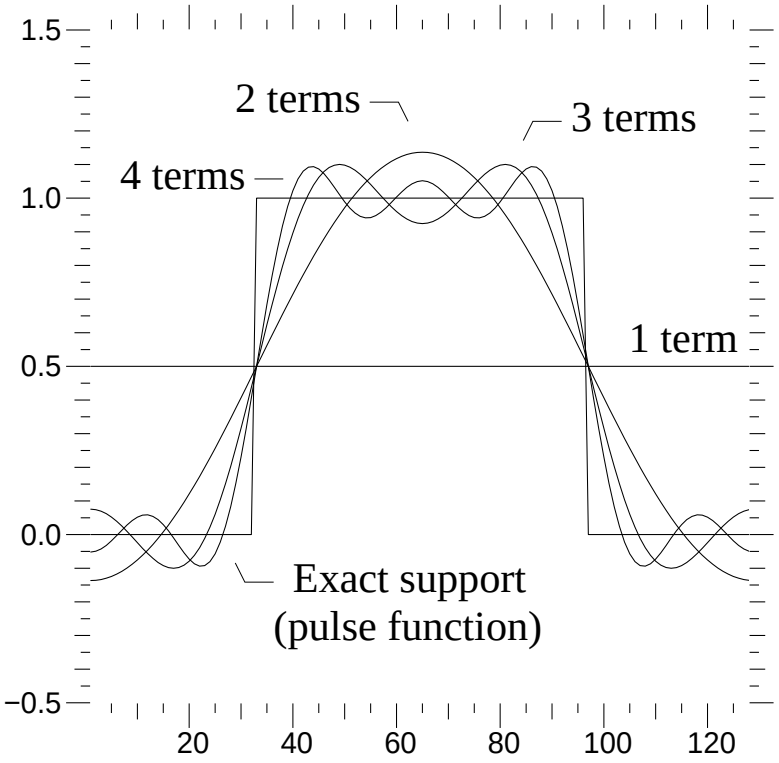

Figure 4.3: The first few terms of the expansion of a 1-D support function (a pulse of lenght N and height 1.)

that the use of other supports gives different interaction functions. We now consider an expansion via Fourier series of a square support like the one in Fig. 4.1. For a 1-D pulse function height 1 and length L within an interval of length $2L$ centered at the origin (see Fig. 4.3) we obtain

$$S(x) = \frac{1}{2} + \sum_{n=1}^{\infty} \left(\frac{2}{n\pi}\right) \sin\left(\frac{n\pi}{2}\right) \cos\left(\frac{n\pi x}{L}\right). \tag{4.9}$$

The discrete version, S_x, where $x = 1, \ldots, N$, is simply obtained by substituting N for L and taking the sum up to only $N - 1$. A 2-D square support can be formed by the product $S_x S_y$.

Let ψ_P be a system of size $(2N)^2$ consisting of four identical objects of size N^2 like

the one in Fig. 4.1-(a) embedded one in each corner. A system similar to the one in Fig. 4.1a can be obtained taking the product of ψ_P with a window $S = S_x S_y$ in one of the corners of the system. In the case where S is an exact square support function (all terms of the series are considered), the part of ψ_P that lies outside the window has no effect in the intensity pattern. This should also hold approximately if enough terms of the expansion of S are taken into account. We define our system as

$$\psi_S = S\,\psi_P. \tag{4.10}$$

Taking the Fourier Transform and applying the Convolution Theorem we have

$$\hat{\psi}_{S\,k_x,k_y} = \frac{1}{2N}\sum_{k_{x\prime}=0}^{2N-1}\sum_{k_{y\prime}=0}^{2N-1}\hat{S}_{k_x-k_{x\prime}}\hat{S}_{k_y-k_{y\prime}}\hat{\psi}_{P\,k_{x\prime},k_{y\prime}}. \tag{4.11}$$

Here $\hat{S}_{k_x}$ and $\hat{S}_{k_x}$ are the 1-D DFTs of S_x and S_y respectively. We now take S_x S_y to be expansions of the pulse function up to the *m-th* term. We obtain the DFT as the sum of the DFTs of each term. This gives us

$$\begin{aligned}\hat{S}_k^{(m)} = \sqrt{2N}\left\{\frac{1}{2}\delta_{k,0}+\right.\\ \left.+\sum_{l=1}^{m}\left(\frac{2}{l\pi}\right)\sin\left(\frac{l\pi}{2}\right)(\delta_{k,l}+\delta_{k,-l})\right\}.\end{aligned} \tag{4.12}$$

The Kroeneker delta terms in Eq. (4.12) correspond to the terms that survive in the sums of Eq. (4.11) -the neighbors of mode $\mathbf{k}$. It is interesting to note that the number of terms taken into account in the expansion of S determines the range of interaction between modes. Before rewriting explicit instances of Eq.(4.11) using (4.12) we state

a few relations that can be derived from the way the system ψ_P is constructed:

$$\begin{aligned}\hat{\psi}_{P\,2k_x,2k_y} &= 2\hat{\psi}_{k_x,k_y} \\ \hat{\psi}_{P\,2k_x+1,2k_y} &= \hat{\psi}_{P\,2k_x,2k_y+1} = \hat{\psi}_{P\,2k_x+1,2k_y+1} = 0.\end{aligned} \tag{4.13}$$

As a reminder, $\hat{\psi}_{k_x,k_x}$ corresponds to the DFT of only one (any) of the copies of the object in ψ_P. From (4.13) it is clear that knowledge of the *e*-*e* amplitudes and phases of $\hat{\psi}_P$ is enough information to obtain $\hat{\psi}$ whose inverse DFT gives us the object (or image). The sum in (4.11) is also simplified by the fact that all even terms are zero ($\sin(\pi l) = 0$). The next step is choosing the number of terms to be taken into account into the expansion of $S_{x,y}$ and obtaining explicit results for (4.12). In this work we have considered up to the third order in the expansion of $S_{x,y}$. We have empirically found that this leads to a good compromise between having a reasonably good approximation of the support and keeping the task of numerically solving the resulting equations feasible. In the case of a first order expansion we obtain

$$\hat{\psi}_{S\,2k_x,2k_y} = \frac{1}{4}\hat{\psi}_{P\,2k_x,2k_y} \tag{4.14}$$

$$\hat{\psi}_{S\,2k_x,2k_y+1} = -\frac{2i}{\pi}\left(\hat{\psi}_{S\,2k_x,2k_y} - \hat{\psi}_{S\,2k_x,2k_y+2}\right) \tag{4.15}$$

$$\hat{\psi}_{S\,2k_x+1,2k_y} = -\frac{2i}{\pi}\left(\hat{\psi}_{S\,2k_x,2k_y} - \hat{\psi}_{S\,2k_x+2,2k_y+1}\right) \tag{4.16}$$

$$\begin{aligned}\hat{\psi}_{S\,2k_x+1,2k_y+1} = -\frac{4}{\pi^2}\Big(&\hat{\psi}_{S\,2k_x,2k_y} - \hat{\psi}_{S\,2k_x,2k_y+2} \\ &-\hat{\psi}_{S\,2k_x+2,2k_y} + \hat{\psi}_{S\,2k_x+2,2k_y+2}\Big).\end{aligned} \tag{4.17}$$

As with (4.5-4.7), one can take the moduli of Eqs. (4.15-4.17) for each non *e*-*e* mode and solve for the *e*-*e* phases of $\hat{\psi}_S$. In fact this can be done easily, since only two

phases are involved in each equation (four for (4.17)). Therefore, given a reference phase (that of the central mode **k** for instance) one can obtain all other phases by propagation. For this work, however, we consider the inclusion of the next two terms in the expansion of the support function, given that this yields a significantly better approximation of the square support as shown in Fig 4.4. The resulting equations for non *e*-*e* modes ((4.14) still holds) are:

$$\hat{\psi}_{S\,2k_x,2k_y+1} = i \sum_{n=-2}^{3} c_n \hat{\psi}_{S\,2k_x,2k_y+2n} \tag{4.18}$$

$$\hat{\psi}_{S\,2k_x+1,2k_y} = i \sum_{n=-2}^{3} c_n \hat{\psi}_{S\,2k_x+2n,2k_y} \tag{4.19}$$

$$\hat{\psi}_{S\,2k_x+1,2k_y+1} = -\sum_{n=-2}^{3}\sum_{m=-2}^{3} C_{m,n} \hat{\psi}_{S\,2k_x+2m,2k_y+2n}. \tag{4.20}$$

The vector of coefficients **c** is given by $c^T = (2/\pi)[-1/5, -1/3, -1, 1, 1/3, 1/5]$ and $C_{m,n} = c_m c_n$. Figure 4.5 gives a schematic representation of equations (4.18-4.20). The range of interaction in this case includes three *e*-*e* neighbors to each side of the *e*-*o* (or *o*-*e*) modes and 36 around the *o*-*o* modes. Again, taking the moduli of the non *e*-*e* modes gives us the equations to obtain (in principle) the unknown phases of the *e*-*e* modes. However, because the interaction is now deeper, the coupling of the nonlinear equations is stronger and the system is harder to solve than for the first order expansion. Fortunately the method we introduce here involves solving a fixed (and relatively small) number of algebraic equations that does not depend on the size of the system.

We consider a square subsystem of 17×17 modes in reciprocal space, centered at the origin ($\mathbf{k} = 0$). Within this system there are 81 phases (the phases of the *e*-*e*

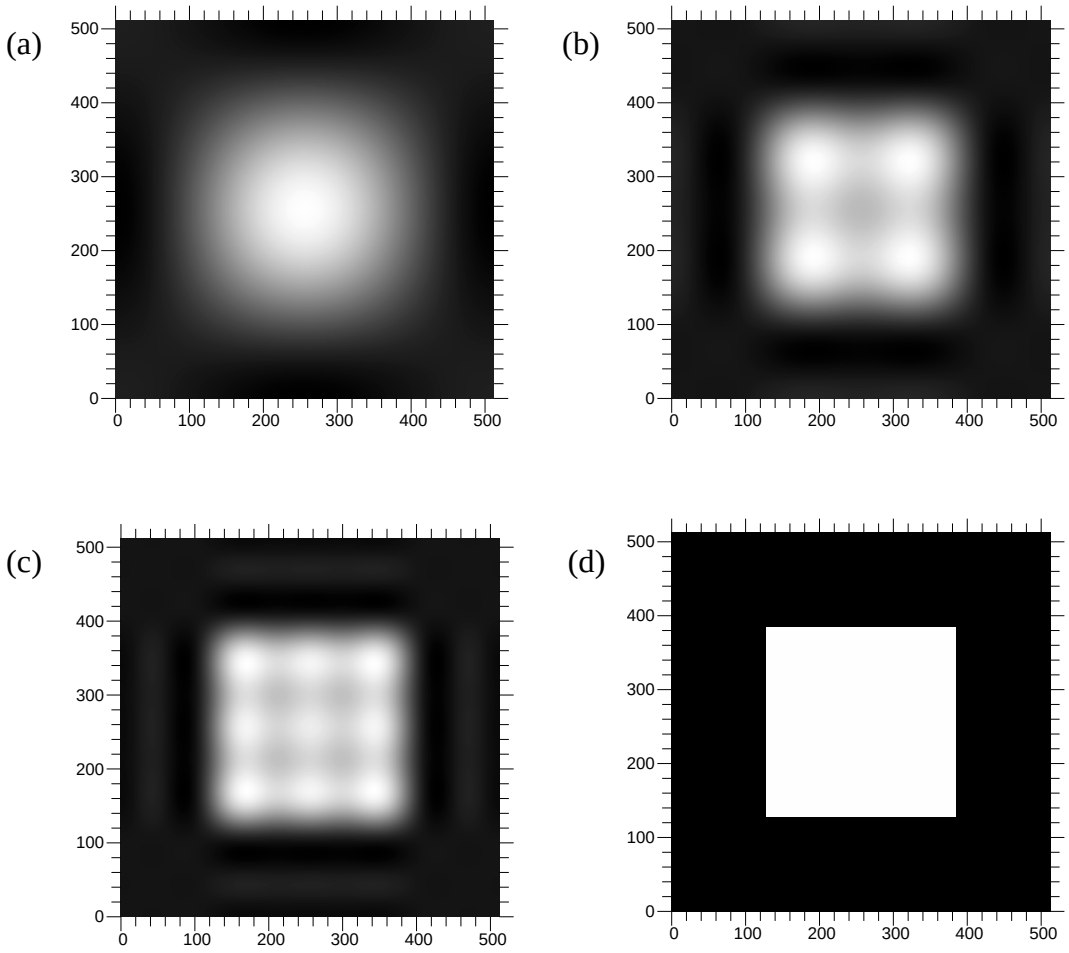

Figure 4.4: First (a), second (b) and third (c) order expansions of the support function in 2D. (d) Corresponds to the exact support function.

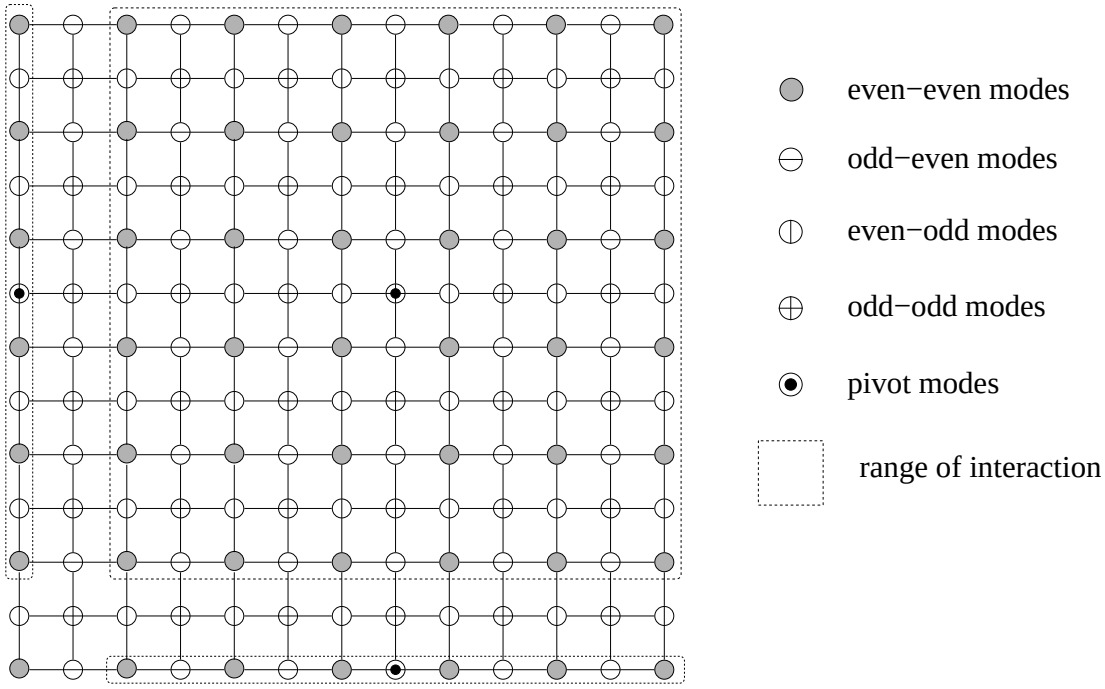

Figure 4.5: Graphical representation of the dependence of non *e*-*e* modes on *e*-*e* *modes* (grey locations). The *e*-*e* modes enclosed in the marked regions are the ones that determine the value of chosen *pivot* modes via Eqs. (4.18-4.20). Each type if equation (horizontal, vertical, and combined) is represented.

modes) whose specification determines the remaining modes via equations (4.19-4.20). Yet, because of Friedel's law only 40 of this 81 phases are independent (the phase of the central mode is assumed to be known). We also find exactly 40 independent equations within this system which can be horizontal (o-e), vertical (e-o) or combined (o-o). With this in mind we are able to split the solution of the problem in two stages (Fig. 4.6). In the first (core) stage, the 40 central independent phases are found using 40 independent equations of the form (4.18-4.20), this is the difficult part because all equations are nonlinear and we need to use a numerical method to solve it. The second (propagation) stage consists of applying the vertical (4.18) and horizontal (4.19) equations successively to find the phases outside of the central subsystem. This can be done in a much easier way because one needs to solve for only one variable in each equation. In the next section we briefly describe how we apply this two stage method to retrieve the phase of a sample system.

4.2 Results

We applied the method described in the last section for a system that consists of the object in Fig. 4.1 embedded in the support of Fig. 4.4(c) (see Fig. 4.7). The simulated intensity was obtained by taking the DTF of the system, and the resulting amplitude values were used as the only available data.

As we mention above, the number of unknowns (and equations) to solve for in the first stage does not depend on the size of the system. Instead it is fixed by the number of terms taken into account in the expansion of the support function. For the first stage, the system of equations is obtained by taking all possible (horizontal, vertical and combined) independent equations of the form of (4.18-4.20) that contain

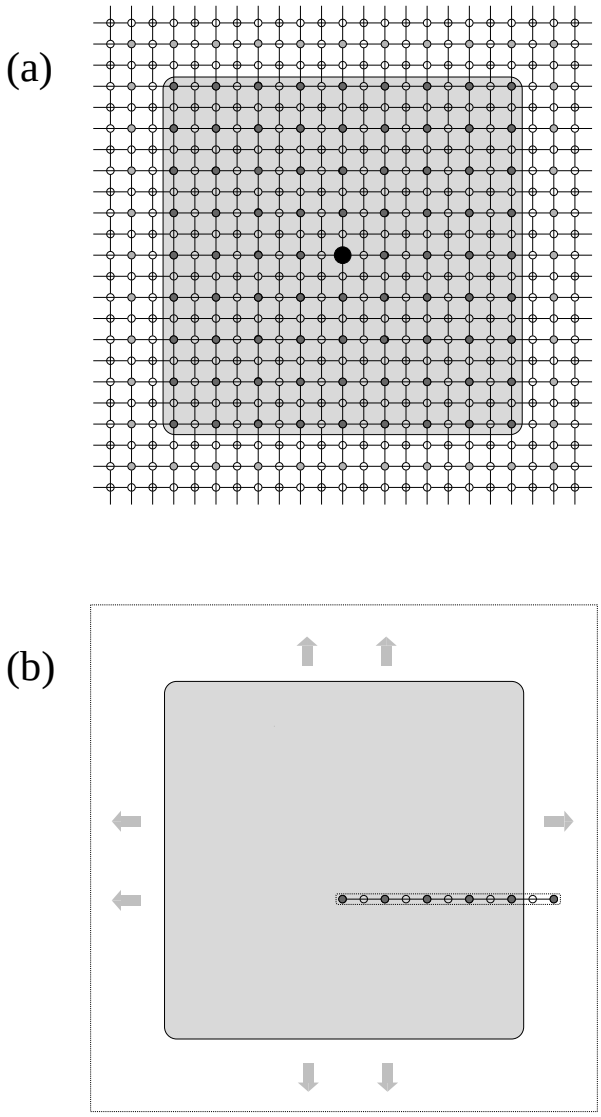

Figure 4.6: Two-stage method for obtaining the phases of the *e*-*e* modes (which is enough to determine the structure of the object). In the first stage (a) a region of fixed size (grey area) is selected around mode $\mathbf{k} = 0$ (central black dot). Within this region there are exactly 40 independent phases and 40 independent equations relating this phases; these equations can be solved numerically. In the second stage (propagation), the value of neighboring *e*-*e* phases outside the core is obtained successively. Note that, in the equation relating 5 phases inside the central region and one outside of it, the latter is the only unknown.

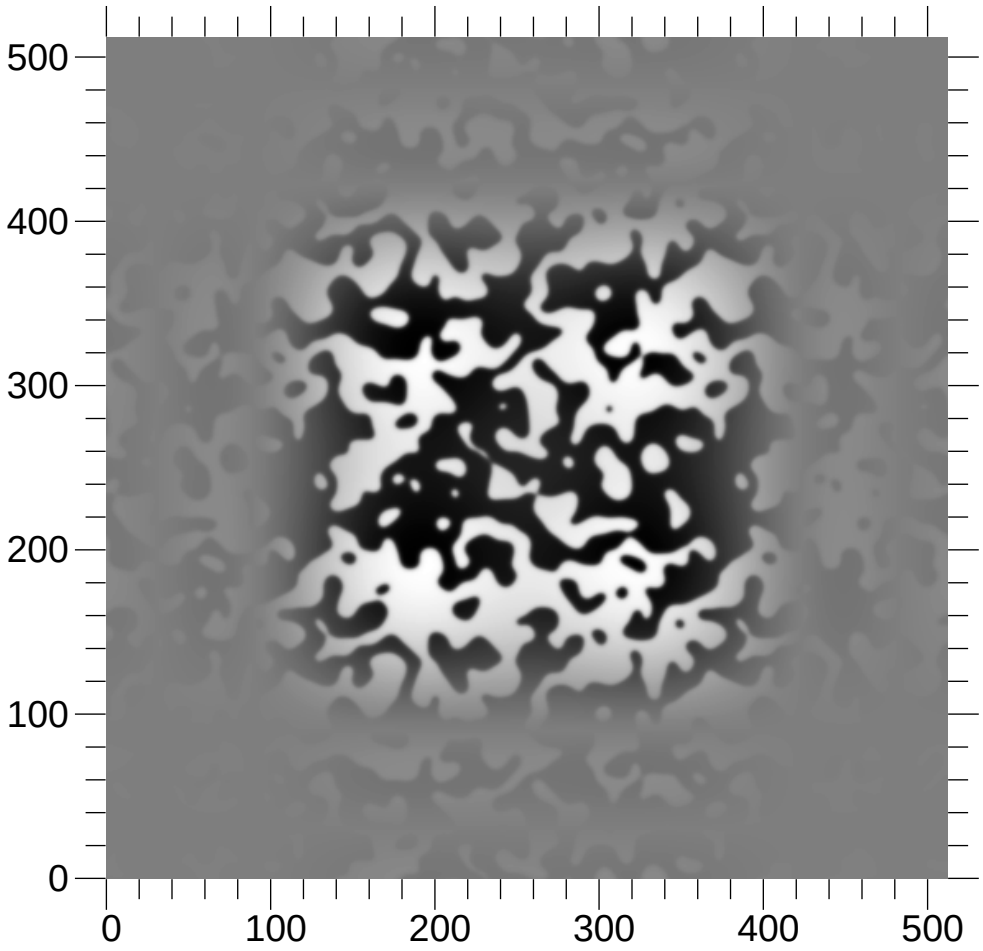

Figure 4.7: Sample pattern for phase retrieval.

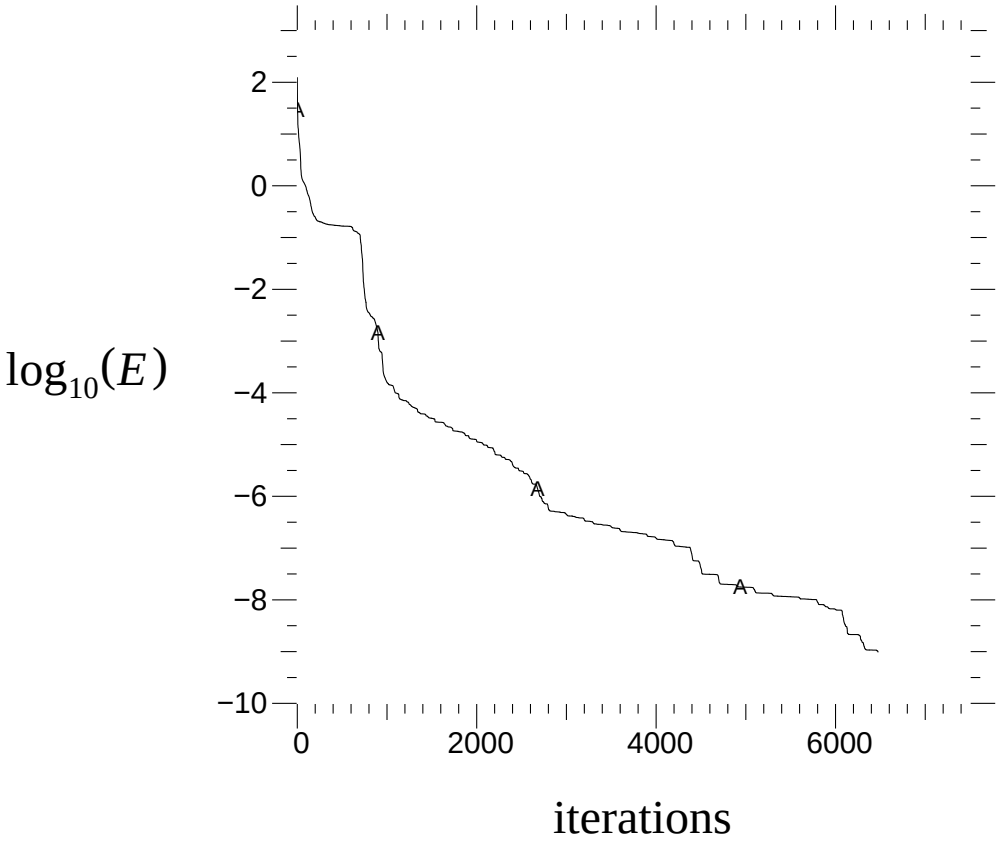

Figure 4.8: Convergence of the error function E for the minimization method (stage 1 of the phase retrieval scheme). A Conjugate Gradients scheme was used in which the Fletcher-Reeves and the Polak-Ribière search directions were alternated every 200 iterations. The vector that minimizes E ($tol = 10^{-9}$) yields the solution of the 40 *core* phases.

all the independent variables (phases) within the central region, and then obtaining the squared modulus for each; this eliminates the unknown phases of the pivot points. It also results in the creation of cosine terms whose arguments are the phase differences between the e-e modes contained in the equation. This equations are nonlinear and cannot be solved by conventional matrix inversion methods. An algorithm such as Newton's method may be applied but we have found that, for this particular case it tends to be numerically unstable unless we start with a very good initial estimate. Our approach was to transform the system of equations into a minimization problem. Since the resulting objective function is analytical, gradient search methods such as Steepest Descent or Conjugate Gradients can be applied. However, as it is expected from the non-linearity of our equations, local minima, which correspond to false solutions, are encountered. To tackle this problem we took a set of different starting points (picked randomly); and then chose the solutions that yielded the smallest values for the objective function after minimization (those below an arbitrary, pre-defined tolerance) to ensure that we found a global minimum. For our objective function we found the best results by applying a scheme using the Conjugate Gradients method; and alternating between the Fletcher-Reeves [36] and the Polak-Ribière [37] search directions every few iterations. Figure 4.8 shows the convergence rate of the objective (error) function for a "good" starting point. We found that typically 1/20 of the initial guesses converged to global minima. The vector of 40 phases found to minimize the objective function was used in the propagation stage to find the rest of the phases.

Chapter 5

Phase retrieval for ordering systems

In this chapter we are concerned with the time dependence of the Fourier transform phase of coherently scattered radiation from a system undergoing ordering. Specifically, we derive a simple model that takes into account the known scaling laws for ordering dynamics to predict the statistical behaviour of the Fourier transform phase. We consider a two-dimensional system of domains undergoing ordering for both the non-conserved and conserved order parameter cases (models A and B respectively). In section 5.2, predictions from our model are compared with numerical experiments where a time dependant Ginzburg-Landau equation is integrated to compute the dynamics of the real-space system; then a simple numerical (discrete) Fourier Transform is applied to compute the Fourier phase as well as the amplitude (directly related to scattering intensity). An average phase-decorrelation time (the average time it takes for the phase to change by a specific amount) is obtained using both our theoretical model and the numerical results. In section 5.3, this quantity is used to implement a

phase-retrieval strategy that consists of measuring scattering intensities of the same non-equilibrium system at different times, and then applying an iterative phase retrieval algorithm (like Fienup's Hybrid Input-Output) recursively with improved initial estimates for faster convergence and higher convergence rates. In the following section we present the derivation of our model. The content of this chapter is based in the work presented in Ref. [38].

5.1 Model

We begin by deriving a simple model to obtain the standard deviation of the phase change between two times of the domains evolution for ordering dynamics. Let there be a system described by order parameter $\psi(\mathbf{r}, \tau)$. We consider ordering after a symmetric quench into the coexistence region. In the late time regime, where domains are well defined and of size considerably larger compared to the thickness of interfaces, the value of ψ at a point within one of the domains can be approximated by the equilibrium value of that order parameter under the present set of conditions. For instance, let $\pm\psi_{eq}$, with $\psi_{eq} > 0$, be the equilibrium value of the order parameter, then we consider $\psi(\mathbf{r}, \tau) \simeq \pm\psi_{eq}$ everywhere except at the interfaces. Furthermore, we neglect the interface thickness.

Within this approximations we take our system to be described by the field $\psi(\mathbf{r}, \tau)$, which can take only the values $\pm\psi_{eq}$. Let $\hat{\psi}(\mathbf{k}, \tau)$ be the spacial 2D Fourier transform of $\psi(\mathbf{r}, \tau)$. We can write $\hat{\psi}$ in terms of its modulus A and phase ϕ,

$$\hat{\psi}(\mathbf{k}, \tau) = A(\mathbf{k}, \tau) e^{\phi(\mathbf{k}, \tau)}. \tag{5.1}$$

As mentioned in section 2.3, at late times of the evolution of domains, the statistical properties of the system depend on time only through a characteristic length, $R(t)$. This quantity corresponds to the average domain size.

Within our approximations, both the magnitude and argument of the Fourier transform are fully determined by the position of the interfaces. Hence the motion of the interfaces completely determines the time evolution of both modulus and phase. With this in mind we have constructed the simplest possible model that both allows for some analysis and roughly preserves the same features of the real domains in terms of interface motion. We describe this model below, mentioning a few important approximations along the way.

We define our model system, $\psi_0(\mathbf{r}, \tau)$, to be a set of non-intersecting 2D circles with their centres randomly distributed and with sizes obeying the following time-dependent distribution:

$$n(\kappa) = \alpha\kappa\rho(\kappa), \tag{5.2}$$

where, α is a proportionality constant $n(\kappa)$ is the proportion of circles of curvature κ (radius $r = 1/\kappa$) and $\rho(\kappa)$ is the curvature distribution of the true system, defined in such way that $\rho(\kappa)d\kappa$ is proportional to the total interface length of curvature κ and $\kappa + d\kappa$. The proportionality constant in Eq. (5.2) can be obtained via the normalisation of $n(\kappa)$ which gives $\alpha = 1/\langle\kappa\rangle = R$.

We now take the Fourier Transform of $\psi_0(\mathbf{r})$. Since this is a linear operator, we can define the quantity $\delta\hat{\psi}_0(\mathbf{k}, \kappa)$ as the partial Fourier Transform of all circles of curvature between κ and $\kappa + d\kappa$. The value of $\psi_0(\mathbf{k})$ is then:

$$\hat{\psi}_0(\mathbf{k}) = \int_0^\infty n(\kappa)\delta\hat{\psi}_0(\mathbf{k}, \kappa)d\kappa. \tag{5.3}$$

In a finite system (because the number of circles is a discrete quantity) the integral in Eq. (5.3) must become a sum.

Our next approximation is that the distribution $n(\kappa)$ is sufficiently sharp and dominated by the mean. In this case $n(\kappa) = \delta(\kappa - \langle\kappa\rangle)$ and $\hat{\psi}_0(\mathbf{k}) = \hat{\psi}_0(\mathbf{k}, \kappa)$. Given now that all circles are assumed to be of radius $R = 1/\langle\kappa\rangle$ our model system $\psi_0(\mathbf{r}, \tau)$ is described by only R and the set $\{\mathbf{r}_j\}$ representing the positions of the centres of the circles. Ignoring the constant background term, whose Fourier transform gives a term proportional to $\delta(\mathbf{k})$, we have, for $k \neq 0$,

$$\hat{\psi}_0(\mathbf{k}; R, \{\mathbf{r}_j\}) = 2\psi_0 \sum_j \hat{\Pi}(\mathbf{k}; R, \mathbf{r}_j), \tag{5.4}$$

where,

$$\Pi(\mathbf{r}; R, \mathbf{r}_j) = \begin{cases} 1, & \text{if } |\mathbf{r} - \mathbf{r}_j| \leq R \\ 0, & \text{otherwise,} \end{cases} \tag{5.5}$$

corresponds to a circular step function of radius R, centered on $\mathbf{r}_j$. Its Fourier transform is proportional to the Bessel function of the first kind and order one, J_1 with a phase factor determined by the value of $\mathbf{r}_j$:

$$\hat{\Pi}(\mathbf{k}; R, \mathbf{r}_j) = \frac{2\pi R}{k} J_1(kR) e^{i\mathbf{k}\cdot\mathbf{r}_j}. \tag{5.6}$$

Substituting Eq. (5.6) into Eq. (5.4) we get

$$\hat{\psi}_0(\mathbf{k}; R, \{\mathbf{r}_j\}) = \frac{4\pi\psi_0 R}{k} J_1(kR) \sum_j e^{i\mathbf{k}\cdot\mathbf{r}_j}. \tag{5.7}$$

The phasor sum on Eq. (5.7) becomes a random walk in 2D if the positions $\{\mathbf{r}_j\}$

are randomly distributed. Next, we consider a small displacement of the interface, which in our model system corresponds to an expansion or contraction of the circles that constitute it. It is important to stress at this point that we are not modelling our real systems domains to be ψ_0. Rather, we are modelling the displacement of the domains interfaces within a short period of time (for the purpose of phase change) as if it were approximately given by the displacement of the interfaces in our model system. We consider the simplest case of interface displacement that produces an argument change in our model system, which is the uniform expansion or contraction of circles. To first order, we consider that displacement to be given, in average, by the change in characteristic domain size δR within a short time $\delta\tau$. Thus each circle is allowed to either randomly contract or expand (but not displace) by $\delta R_j = \pm|\delta R|$. The resulting change in ψ_0 is given by

$$\begin{aligned}\delta\hat{\psi}_0(\mathbf{k}; R, \{\mathbf{r}_j\}) =& \hat{\psi}_0(\mathbf{k}; \{R + \delta R_j\}, \{\mathbf{r}_j\}) \\ &- \hat{\psi}_0(\mathbf{k}; R, \{\mathbf{r}_j\}) \\ =& 4\pi\psi_0 R J_0(kR) \sum_j e^{i\mathbf{k}\cdot\mathbf{r}_j}\delta R_j \end{aligned} \tag{5.8}$$

for small values of $|\delta R_j|$. Since the signs of δR_j are random, the sum in Eq.(5.8) is also a random walk but independent to that of Eq. (5.7). Seeing both $\hat{\psi}_0$ and $\delta\hat{\psi}_0$ as statistically independent phasors and knowing the variance of the magnitude of each, we can estimate the variance of the argument difference $\delta\phi$:

$$\langle\delta\phi^2\rangle \approx 2\left(\frac{\langle|\delta R|\rangle}{R}\right)^2. \tag{5.9}$$

To obtain Eq. (5.9) we have, in addition, taken only the lowest order terms in

the expansion of both J_0 and J_1, thus making it only valid for $kR \ll 1$ (small wavenumbers). Note that, for that limit, the above expression is no longer dependent on k. Now we substitute the time dependence into R and δR, given by $R = [B\tau]^n$ and $\delta R \simeq (dR/d\tau)\delta\tau = nB^n\tau^{n-1}\delta\tau$. Substituting in Eq. (5.8), we get

$$D(\tau, \delta\tau) \equiv \langle \delta\phi^2 \rangle^{1/2} = \beta n \bar{\tau}^{-1} \delta\tau, \tag{5.10}$$

where $\bar{\tau}$ is the average time within the interval $\delta\tau$ and β is a proportionality constant. Equation (5.10) gives us the RMS value of the change in argument as a function of time. It should be valid for small time intervals and small values of kR. Even though many approximations were made in its derivation, equation (5.10) is in fairly good agreement with our numerical results as will be seen in the following sections.

5.2 Numerical Work

In this section we obtain, via numerical simulations, a few important properties to describe the time evolution of the Fourier transform phase during phase separation. To obtain ensemble averages of quantities, we perform a set of simulations for systems undergoing phase-ordering after a temperature quench into a coexistence region, varying only initial conditions determined by thermal noise. We consider the dynamics described by both a non-conserved (Model A) and a conserved (Model B) order parameter. For each case we use a deterministic equation that can easily be integrated in time using Euler's method. The derivation of this equation as well as the details of the integration procedures are identical those presented in Ref. [39] for Model A and Ref. [40] for Model B. As is done in both of these references, thermal noise is neglected

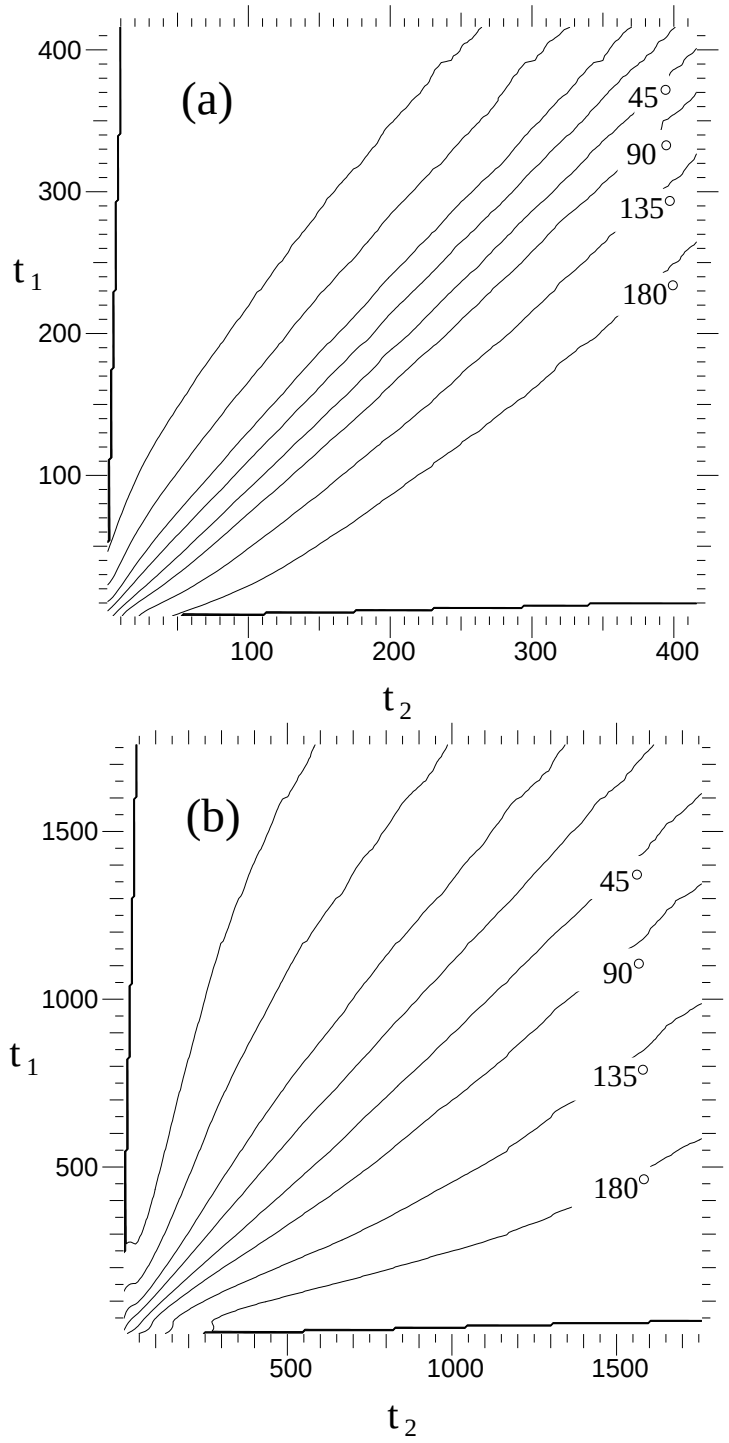

Figure 5.1: Contour plots of scaled phase decorrelation function, $C(t_1, t_2)$. (a) Model A (non-conserved) dynamics. (b) Model B (conserved) dynamics. Note that plots are symmetric about the $t_1 = t_2$ line since $C(t_2, t_1) = C(t_1, t_2)$.

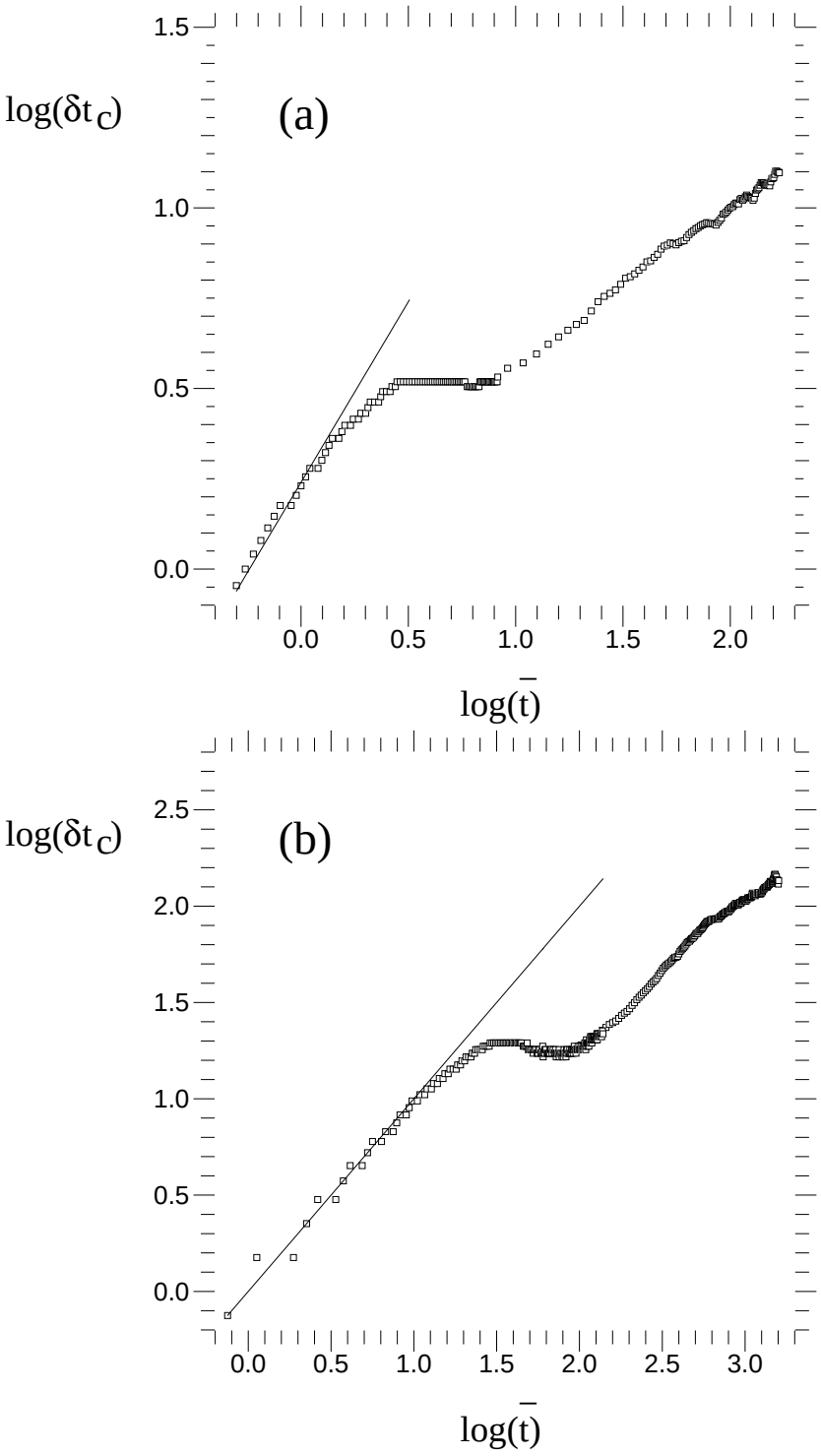

Figure 5.2: Characteristic time difference $log(\delta t_c)$ for $D = \langle \delta\phi^2 \rangle^{1/2} = 45^\circ$ as a function of average time, $log(\bar{t})$. For both plots, Model A (a) and Model B (b), the fit for early times (left solid line) has a slope of ≈ 1, which gives $\delta t_c \propto \bar{t}$.

throughout the domains' evolution and the source of randomness is the initial state.

In Refs. [39] and [40], intensity is calculated from the Fourier transform modulus in simulations of phase-ordering dynamics. These results are used to compute the two-time covariance correlation functions to characterise intensity (speckle) fluctuations from the average (whose behavior is well known). In the case of the phase, which is not measurable, its average value (at any time) has no physical meaning; it is only useful when it is known at a particular instance. However the average rate of change of the phase in time is a useful quantity since it is related to the real space evolution of the domains. In this work we compute what we define as the phase decorrelation function:

$$C_{\mathbf{k}}(\mathbf{k}, \tau_1, \tau_2) = \langle (\phi(\mathbf{k}, \tau_1) - \phi(\mathbf{k}, \tau_2)) \rangle^{1/2}. \tag{5.11}$$

As expected, this quantity can also be collapsed into a scaling function dependent only on scaled times $t_i = Bk^{1/n}\tau_i$ at the late stages of phase-ordering: $C_{\mathbf{k}}(\mathbf{k}, \tau_1, \tau_2) = C(t_1, t_2)$. By construction $C(t, t) = 0$, and increases as Δt increases.

To compute $C(t_1, t_2)$, all simulation parameters (except system size; we took 512) were kept identical to those used in Refs. [39] and [40] to facilitate comparison of results. The contour plot of the square root of $C(t_1, t_2)$ for models A and B is presented in figure 5.1. These plots are similar to those of two time intensity covariance presented in Refs. [39] and [40]. Following their approach, we also substitute t_1 and t_2 by the more natural variables: time average $\bar{t} = (t_1 + t_2)/2$ and time difference $\delta t = |t_2 - t_1|$. We also define a '*characteristic*' value δt_c that corresponds to the time difference at which $\langle \delta\phi^2 \rangle^{1/2}$ has a definite value. In figure 5.2 we plot (again for model A and model B) the characteristic time difference vs. average time for $\langle \delta\phi^2 \rangle^{1/2} = 45^\circ$. We can see that for both cases, at small average times δt_c increases linearly with time.

This result agrees with the one obtained with our model on the previous section (note that Eq. 5.10 remains unchanged if we use rescaled time t instead of τ). Below, this result is used to obtain time intervals for which the angle decorrelation is constant, as this helps us choose optimal "snapshots" of the system for phase retrieval.

5.3 Results

We now present an example where we incorporate the results obtained in the previous section into our phase retrieval strategy. The way we proceed is essentially by generating a series of simulated intensity "snapshots" at time intervals determined with the use of Eq. (5.10). These "snapshots" represent measurements at different times of a single undergoing domain growth. We let $\{\tau_j\}$; $j = 1, 2, ...N_s$ be the set of (rescaled) times at which these snapshots are taken. They are chosen the following way: the first time τ_1 of the series is chosen to be any time within the late-stage growth regime (where scaling applies and domains are well defined). The next step is to apply Eq. (5.10) recursively (having chosen a value for the constant β and for D) to obtain the rest of the time series. The last time of the series should be one for which the system possesses a well-defined and relatively simple structure; simple enough to be easily reconstructed (without stagnation) by a standard phase retrieval method like HIO regardless of the initial guess employed. In the following sample run, where we consider domain growth (Model A) in a 2D system of size 256×256. We let $D = 45^\circ$ and we obtain the value of β from the plot of Fig. 5.2-(b). In the form of a recursive relation, Eq. (5.10) (recall that under the approximations of our

model, Eq. (5.10) holds for both τ and t) reads:

$$\tau_{n+1} = \gamma\tau_n, \tag{5.12}$$

where $\gamma = (2+\epsilon)/(2-\epsilon)$ and $\epsilon = D\beta/n$. Equation (5.12) shows the times $\{\tau_j\}$ constitute a geometric series. Empirically, we found $\tau_1 = 12.5$ and $\tau_N = 500$ to be appropriate initial and final times. For the value of $\gamma \simeq 1.2$ obtained from the graph, we found that approximately 22 time frames cover the entire time interval. The value of γ was slightly adjusted to $\simeq 1.193$ so that the final frame corresponds to $\tau = 500$.

For the final intensity frame, we applied Fienup's HIO algorithm (details of its implementation are are given in Ref. [10]) with finite, tight support constraints to retrieve the image $\psi(\mathbf{r})$. As initial input image we used a set of random numbers uniformly distributed between $-\psi_{eq}$ and ψ_{eq}. In what follows, we refer to this initial random guess as random input. Once the phase (and therefore) the image at τ_N was found. We used this image as input (initial estimate) for the HIO algorithm at τ_{N-1}. Because we expect some degree of correlation between the phase at these two times, the input ψ_N must be a better estimate than a random one. Indeed, as we show below, the convergence of the algorithm is much faster in the former case. We repeat this procedure recursively for all time-frames until we get to τ_1. In figure 5.3 we compare the error metric (ε) convergence curves obtained with this strategy to the same curves obtained from random inputs. We pick sample intensity snapshots (we show the corresponding order parameter images instead) at four different times between (and including) τ_1 and τ_N. We found, as Fig. 5.3 shows, that using the strategy we propose above, drastically reduces convergence time for each sample. An interesting finding is that the improved initial estimate (IIE) convergence curves are

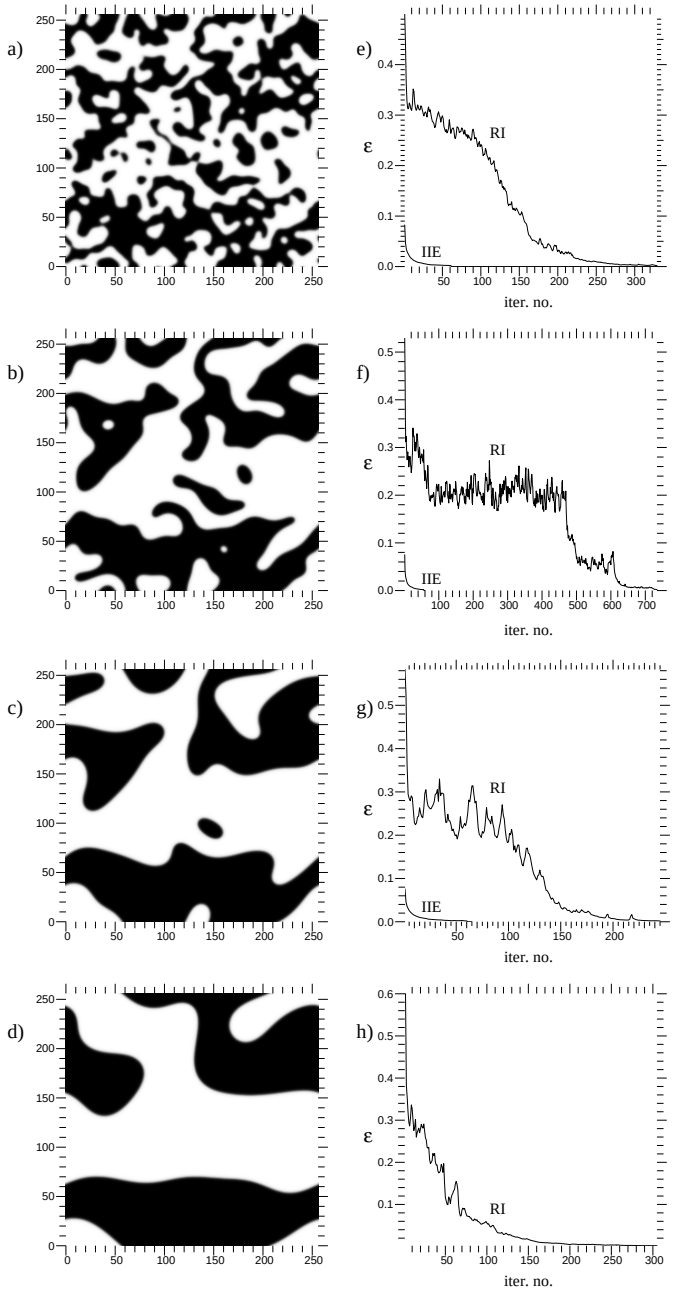

Figure 5.3: Patterns of domain growth (model A) after temperature quench, at four different times: (a) $\tau = 12.5$, (b) $\tau = 35.8$, (c) $\tau = 122.8$ and (d) $\tau = 500$. (e)-(h) Error metric, ε vs. number of iterations for phase retrieval of the corresponding patterns on the left. Convergence curves for random inputs (RI) are compared with those using improved initial estimates (IIE).

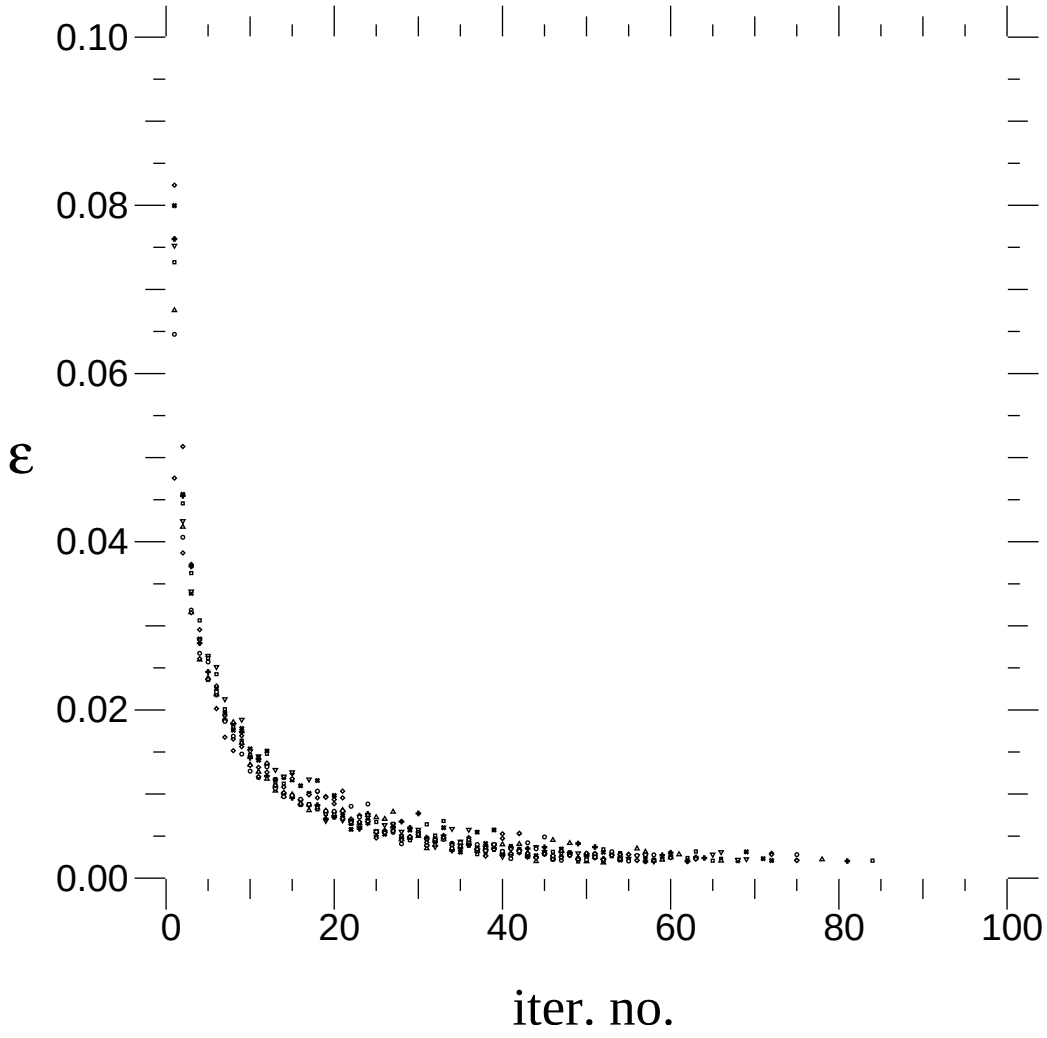

Figure 5.4: Overlap of convergence curves, from improved initial estimates, corresponding to different times. Error metric, ε vs. number of iterations.

all approximately the same (they overlap) for different times. Fig. 5.4 shows ensemble averages of IIE curves for the same set of times shown in Fig. 5.3. Collapse of the data to a single curve is apparent. Empirically we found the best fit to this curve to be a stretched exponential.

We have also studied the effect of the time sampling rate, which is determined by the parameter γ. Our results are presented in Fig. 5.5, which was obtained the following way: We computed an ensemble of 20 samples of ordering systems with model A dynamics after a temperature quench from different random initial states. For all samples, we took the patterns at $\tau_0 = 12.5$ and $\tau_f = 500$ as, respectively, the initial and final sampling times. We then varied the number of intensity snapshots (N_s) to be taken between τ_0 and τ_f and computed the corresponding value of γ,

$$\gamma = \left(\frac{\tau_f}{\tau_0}\right)^{\frac{1}{N_s+1}}. \tag{5.13}$$

The intensity sampling times for each series were obtained using Eq. 5.12. For each value of gamma, the total number of Fienup's HIO steps required to recursively obtain $\psi(\mathbf{r}, \tau_0)$ from $\psi(\mathbf{r}, \tau_f)$ involving the in-between intensity measurements (as in the method described above) was computed and the ensemble average taken.

The plot of Fig. 5.5 shows how, if we wish to recover only $\psi(\mathbf{r}, \tau_0)$ from $\psi(\mathbf{r}, \tau_f)$, intensity sampling at intermediate times is unnecessary. It also shows that values of γ below ~ 1.007 correspond to excessive sampling. We observed that the reason behind the sharp increase in number of iterations beyond this value is that each sample requires at least one HIO step to converge. We can also notice that there is no significant variation for the computational time between the values $\gamma \sim 1.02$ and $\gamma \sim 1.26$. It is important to keep in mind that the above analysis does not take

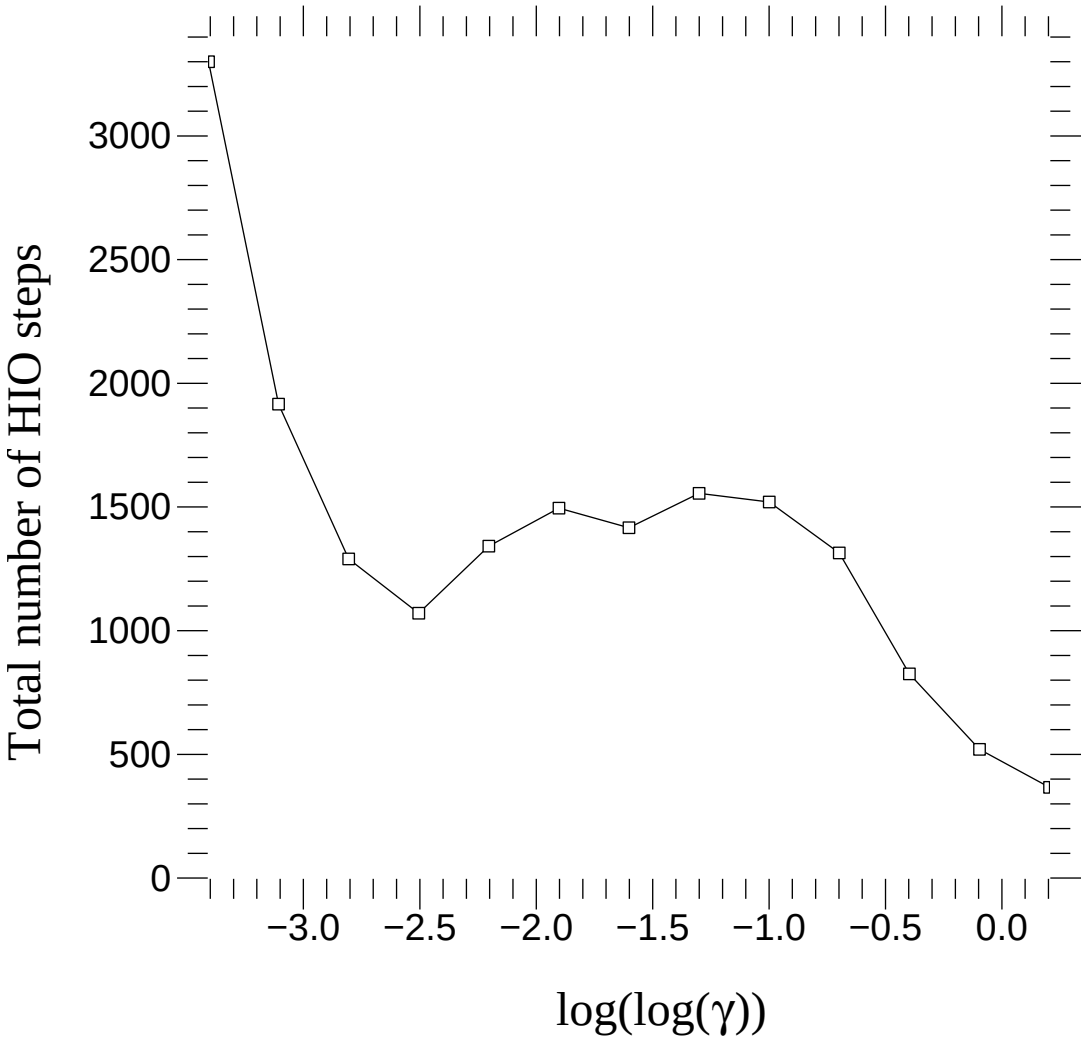

Figure 5.5: Average number of total HIO steps needed to reconstruct a pattern at time $\tau_0 = 12.5$ starting from a pattern at time $\tau_f = 500$ vs. sampling time ratio γ. The largest value of γ corresponds to no intensity samples between τ_0 and τ_f ($N_s = 0$) while the smallest value corresponds to $N_s = 4095$ samples.

into account the extra additional information obtained from the images retrieved at intermediate times, which is one of the reasons our strategy could still be useful in practice.

Chapter 6

Conclusions

Throughout this work, we have studied several topics related to methods for phase retrieval from intensity measurements.

In chapter 3, we presented an algorithm for phase retrieval based on recursive phase propagation from estimated phase differences between Fourier samples for strictly localized images. Our work is based on a higher order correction to an expression obtained by Bates [1–3, 21] to compute phase difference estimates. We showed, through a few examples, how our method yields improved estimates for the phase differences as well as for image reconstructions in 1D. Unfortunately, we have found problems for the application of our algorithm to images in higher dimensions. Specifically, we have observed the presence of "unsteady" states when applying the correction terms for the phase differences to a single Nyquist cell propagation. This is related to the fact that the sign of each actual phase difference is chosen by a "minimum difference between paths" criterion, and that the choice may be wrong if the phase difference estimates are not accurate enough. Although we have not been able to overcome this difficulty, we believe that it should be resolved once better estimates for each phase difference

can be computed at the preliminary propagation stage. Further improvement could be achieved by making the function J_{sl} to be more extended; although this would imply the need for the inclusion of additional unknown phases in the correction term of (3.27). The computational effort required by this method is not significantly greater than that required by Bates's method. For an image consisting of M^d components and a linear oversampling ratio of N in each direction, the time complexity of the algorithm is $O(M^d N^d)$ times the number of iterations required for each Nyquist cell propagation to converge. Empirically, we found this to be $\sim 30-50$, regardless of the values of N and d. Like all recursive propagation algorithms, this one has the drawback of being overly sensitive to both noise in intensity measurements and rapid phase variations, which lead to error buildup. Consequently, it is most likely inappropriate for images with high frequency components. However, it can be readily implemented as a refinement for the "crude phase estimation" stage (followed by "Fienup tidying") of the composite method proposed in [41], given that our approach avoids the stagnation problems associated with the most common iterative algorithms.

A somewhat similar approach was adopted in chapter 4, where we introduced algorithm for phase retrieval from intensity measurements using a special support function which approximates a sharp-edged square support. We showed that, taking a few terms of a Fourier series expansion of the support function, it is possible to reduce the phases that need to be found simultaneously to a number that is independent of the size of the system, which greatly simplifies the solution of the phase problem. We also showed how the remaining phases can be found successively using a propagation method. Unfortunately, we found that the direct implementation for this method for the case of the sharp square support fails because, as the equations no longer hold exactly, their approximate solution via minimization becomes unstable. This

is further worsened by error buildup during the propagation stage. We believe the inclusion of more terms in the expansion of the support may help to solve this problem. In doing this, only the range of interaction between modes and the number of modes that must be determined simultaneously during the first stage is affected. Thus, the generalization of this scheme for an arbitrary number of terms could be an interesting task for future works. Moreover, different support geometries (like circular) and other system/support size ratios could be studied.

In chapter 5 we studied the time dependance of the fluctuations of the Fourier transform phase of a system undergoing ordering. This was achieved by the use of a simple model and through numerical simulations. We found an expression to estimate the time interval for which the phase statistically decorrelates. This time interval depends on the average time between two states of the domains' evolution. We also devised and applied an effective strategy for phase retrieval that greatly reduces the convergence time of a typical algorithm like Fienup's HIO. This can be done by picking intensity "snapshots" at optimally chosen time intervals that are less than the corresponding decorrelation time. Initially, we solve the phase problem for a late time frame, where the domains have coarsened. Then we use the solution as an initial guess for an earlier more complex frame. This is repeated recursively backwards in time. Our method features only one adjustable parameter which determines average angular distance between frames. In a real experiment, this strategy's applicability is limited by the rate at which intensity measurements are available. Unfortunately, as of today, scattering experiments for systems undergoing ordering cannot collect high quality coherent data at the typical rate at which first order transitions occur [42]. In the hope that in the future higher brilliance sources and better detectors become available, the use of experimental data would constitute a good test for the practical

application of our proposed phase retrieval strategy.

References

[1] R. H. T. Bates. Fourier phase problems are uniquely solvable in more than one dimension. I: Underlying theory. *Optik*, 61:247–262, 1982.

[2] K. L. Garden and R. H. T. Bates. Fourier phase problems are uniquely solvable in more than one dimension. II: One-dimensional considerations. *Optik*, 62:131–142, 1982.

[3] W. R. Fright and R. H. T. Bates. Fourier phase problems are uniquely solvable in more than one dimension. III: Computational examples for two dimensions. *Optik*, 62:219–230, 1982.

[4] A. Walther. The question of phase retrieval in optics. *Opt. Acta*, 10:41–49, 1963.

[5] Y. M. Bruck and L. G. Sodin. On the ambiguity of the image reconstruction problem. *Opt. Commun*, 30:304–308, 1979.

[6] M. H. Hayes. The reconstruction of a multidimensional sequence from the phase or magnitude of its Fourier transform. *IEEE Trans. Acoust., Speech, Signal Process.*, ASSP-30:140–154, 1982.

[7] J. Miao and D. Sayre. On possible extensions of x-ray crystallography through diffraction pattern oversampling. *Acta Cryst. A*, 156:596–506, 2000.

[8] R. W. Gerchberg and W. O. Saxton. A practical algorithm for the determination of phase from image and diffraction plane pictures. *Optik*, 35:237–246, 1972.

[9] J. R. Fienup. Reconstruction of an object from the modulus of its Fourier transform. *Opt. Lett.*, 3:27–29, 1978.

[10] J. R. Fienup. Phase retrieval algorithms: a comparison. *Appl. Opt.*, 21:2758–2769, 1982.

[11] V. Elser. Phase retrieval by iterated projections. *J. Opt. Soc. Am. A*, 20:40–55, 2003.

[12] J. R. Fienup and C. C. Wackerman. Phase-retrieval stagnation problems and solutions. *J. Opt. Soc. Am. A*, 3:1897–1907, 1986.

[13] R. G. Lane. Recovery of complex images from Fourier magnitude. *Opt. Commun.*, 63:6–10, 1987.

[14] J. R. Fienup. Reconstruction of a complex-valued object from the modulus of its Fourier transform using a support constraint. *J. Opt. Soc. Am. A*, 4:118–123, 1987.

[15] R. D. Millane. Phase retrieval in crystallography and optics. *J. Opt. Soc. Am. A*, 7:394–411, 1990.

[16] C. H. Spence. Phase recovery and lenseless imaging by iterative methods in optical, x-ray and electron diffraction. *Phi. Trans. R. Soc. Lond. A*, 360:875–895, 2002.

[17] G. B. Arfken and H. J. Weber. *Mathematical methods for physicists*. Harcourt/Academic Press, 2001.

[18] W.O. Saxton. *Computer Techniques for Image Processing in Electron Microscopy*. Academic, New York, 1978.

[19] N. C. Gallagher and B. Liu. Method for computing kinoforms that reduces image reconstruction error. *Appl. Opt*, 12:2328, 1973.

[20] D. Montiel, M. Sutton, and M. Grant. Phase retrieval by propagation for localized images. *J. Opt. Soc. Am. A*, 25:2784–2790, 2008.

[21] R. H. T. Bates. Uniqueness of solutions to two-dimensional Fourier phase problems for localized and positive images. *Comput. Vis. Graph. Image Process.*, 25:205–217, 1984.

[22] J. Miao, P. Charalambous, J. Kirz, and D. Sayre. Extending the methodology of x-ray crystallography to allow imaging of micrometr-sized non-crystalline specimens. *Nature*, 400:342–344, 1999.

[23] I. K. Robinson, I. A. Vartanyants, G. J. Williams, M. A. Pfeifer, and J. Pitney. Reconstruction of the shapes of gold nanocrystals using coherent x-ray diffraction. *Phys. Rev. Lett.*, 87:195505, 2001.

[24] M. A. Pfeifer, G. J. Williams, I. A. Vartanyants, R. Harder, and I. K. Robinson. Three-dimensional mapping of a deformation field inside a nanocrystal. *Nature*, 442:63–66, 2006.

[25] J. Miao, K. O. Hodgson, T. Ishikawa, C. A. Larabell, M. A. LeGros, and Y. Nishino. Imaging whole Escherichia coli bacteria by using single-perticle x-ray diffraction. *Proc. Natl. Acad. Sci. USA*, 100:110–112, 2003.

[26] D. Shapiro, P. Thibault, T. Beetz, V. Elser, M. Howells, C. Jacobsen, J. Kirz, E. Lima, H. Miao, A. M. Neiman, and D. Sayre. Biological imaging by soft x-ray diffraction microscopy. *Proc. Nac. Acad. Sci. USA*, 102:15343–15346, 2005.

[27] P. Thibault, M. Dierolf, A. Menzel, O. Bunk, C. David, and F. Pfeifer. High-resolution scanning x-ray diffraction microscopy. *Science*, 321:379–382, 2008.

[28] C. Song, H. Jiang, B. Amirebekian, L. Peng, R. Sun, S. S. Shah, Z. H. Zhou, T. Ishikawa, and J. Miao. Quantitative imaging of single, unstained viruses with coherent x rays. *Phys. Rev. Lett.*, 101:158101, 2008.

[29] Y. Nishino, Y. Takahashi, N. Imamoto, T. Ishikawa, and K. Maeshima. Three-dimensional visualization of a human chromosome using coherent x-ray diffraction. *Phys. Rev. Lett.*, 102:018101, 2009.

[30] J. D. Gunton, M. San Miguel, and P. S. Sahni. The Dynamics of First-order Phase Transitions. In C. Domb and J. L. Lebowitz, editors, *Phase Transitions and Critical Phenomena*, volume 8. Academic, London, 1983.

[31] P. C. Hohenberg and B. I. Halperin. Theory of dynamic critical phenomena. *Rev. Mod. Phys.*, 49:435, 1977.

[32] A. J. Bray. Theory of phase-ordering kinetics. *Adv. Phys.*, 43:357, 1994.

[33] C. Song, D. Ramunno-Johnson, Y. Nishino, Y. Kohmura, T. Ishikawa, C. Chen, T. Lee, and J. Miao. Phase retrieval from exactly oversampled diffraction intensity through deconvolution. *Phys. Rev. B*, 75:012102, 2007.

[34] K. T. Knox and B. J. Thompson. Recovery of images from atmospherically degraded-short exposure photographs. *Astrophys. J*, 193:L45, 1974.

[35] D. Montiel, M. Sutton, and M. Grant. Localized phase retrieval for oversampled intensity measurements. (Submitted for publication).

[36] R. Fletcher and C. Reeves. Function minimization by conjugate gradients. *Comput. J.*, 7:149–154, 1964.

[37] E. Polak and G. Ribière. Note sur la convergence des méthodes de directions conjuguées. *Rev. Fr. Inform. Rech. Oper.*, 16:35–43, 1969.

[38] D. Montiel, M. Sutton, and M. Grant. Phase retrieval from speckle patterns of ordering systems. (Submitted for publication).

[39] G. Brown, P. A. Rikvold, M. Sutton, and M. Grant. Speckle from phase-ordering systems. *Phys. Rev. E*, 56:6601, 1997.

[40] G. Brown, P. A. Rikvold, M. Sutton, and M. Grant. Evolution of speckle during spinodal decomposition. *Phys. Rev. E*, 60:5151, 1999.

[41] R. H. T. Bates and W. R. Fright. Composite two-dimensional phase-restoration procedure. *J. Opt. Soc. Am.*, 73:358, 1983.

[42] Mark Sutton. Personal communication, 2009.